A TRIDENT SCHOLAR PROJECT REPORT

NO. 507

Freestream Deceleration Effects on Film Cooling Over a Flat Plate

by

Midshipman 1/C Matthew C. Gillcrist, USN

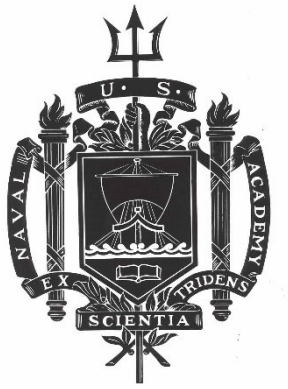

UNITED STATES NAVAL ACADEMY
ANNAPOLIS, MARYLAND

USNA-1531-2

REPORT DOCUMENTATION PAGE

Form Approved
OMB No. 0704-0188

1. REPORT DATE *(DD-MM-YYYY)*	**2. REPORT TYPE**	**3. DATES COVERED** *(From - To)*
7/12/21		

4. TITLE AND SUBTITLE
Freestream Deceleration Effects on Film Cooling Over a Flat Plate

5a. CONTRACT NUMBER

5b. GRANT NUMBER

5c. PROGRAM ELEMENT NUMBER

6. AUTHOR(S)
Gillcrist, Matthew C.

5d. PROJECT NUMBER

5e. TASK NUMBER

5f. WORK UNIT NUMBER

7. PERFORMING ORGANIZATION NAME(S) AND ADDRESS(ES)

8. PERFORMING ORGANIZATION REPORT NUMBER

9. SPONSORING / MONITORING AGENCY NAME(S) AND ADDRESS(ES)
U.S. Naval Academy
Annapolis, MD 21402

10. SPONSOR/MONITOR'S ACRONYM(S)

11. SPONSOR/MONITOR'S REPORT NUMBER(S)
Trident Scholar Report no. 507 (2021)

12. DISTRIBUTION / AVAILABILITY STATEMENT

This document has been approved for public release; its distribution is UNLIMITED.

13. SUPPLEMENTARY NOTES

14. ABSTRACT

Film cooling is a method used within gas turbines to cool the turbine blades by blowing air out of small holes in the blade surface of the blades. This allows the gas turbine to be run at higher internal temperatures, increasing the efficiency and power output of the engine. Regions of the curved turbine blade cause the freestream air flowing around it to accelerate and decelerate. This study seeks to determine the effects of this freestream deceleration on film cooling. The experiments accomplish this by using a flat plane with circular, angled holes in the surface to model a small portion of the gas turbine blade. Measurements were made for a zero acceleration case, and two decelerated cases at acceleration parameters (K), a non-dimensional value representing acceleration magnitude, of -0.50×10^-6 and -0.68×10^-6. Three different blowing ratios (M), ratios of the coolant jet velocity to the freestream airflow velocity, were studied in each case. Results show that freestream deceleration has little to no effect on film cooling effectiveness and Stanton number ratio. This information increases understanding of film cooling and allows models to be made more accurate.

15. SUBJECT TERMS
Turbine, film cooling, freestream, deceleration, coolant jet velocity

16. SECURITY CLASSIFICATION OF:			**17. LIMITATION OF ABSTRACT**	**18. NUMBER OF PAGES**	**19a. NAME OF RESPONSIBLE PERSON**
a. REPORT	**b. ABSTRACT**	**c. THIS PAGE**		63	**19b. TELEPHONE NUMBER** *(include area code)*

U.S.N.A. --- Trident Scholar project report; no. 507 (2021)

FREESTREAM DECELERATION EFFECTS ON FILM COOLING OVER A FLAT PLATE

by

Midshipman 1/C Matthew C. Gillcrist
United States Naval Academy
Annapolis, Maryland

Certification of Adviser Approval

Professor Ralph J. Volino
Mechanical Engineering Department

Acceptance for the Trident Scholar Committee

Professor Maria J. Schroeder
Associate Director of Midshipman Research

USNA-1531-2

Abstract

Film cooling is a method used within gas turbines to cool the turbine blades by blowing air out of small holes in the blade surface of the blades. This allows the gas turbine to be run at higher internal temperatures, increasing the efficiency and power output of the engine. Regions of the curved turbine blade cause the freestream air flowing around it to accelerate and decelerate. This study seeks to determine the effects of this freestream deceleration on film cooling. The experiments accomplish this by using a flat plane with circular, angled holes in the surface to model a small portion of the gas turbine blade. Measurements were made for a zero acceleration case, and two decelerated cases at acceleration parameters (K), a non-dimensional value representing acceleration magnitude, of -0.50×10^{-6} and -0.68×10^{-6}. Three different blowing ratios (M), ratios of the coolant jet velocity to the freestream airflow velocity, were studied in each case. Results show that freestream deceleration has little to no effect on film cooling effectiveness and Stanton number ratio. This information increases understanding of film cooling and allows models to be made more accurate.

Keywords: turbine, film, freestream, deceleration, jet, cooling

Acknowledgements

Thank you to Professor Ralph Volino for serving as my Advisor and taking the time to teach me the complexities of research and the gas turbine film cooling field.

Thank you to Louise Becnel, Steven Galindo, and Dan Rogerson for helping me assemble the apparatus and problem solve through small issues that arose regarding the apparatus.

Thank you to Brandon Stanley, Travis Ball, Mika Koivula, Ben Johnson, and Nick Hlavaty for constructing and assembling the apparatus. You all were very helpful and I appreciate the time and craftsmanship put into the apparatus.

Table of Contents

Introduction

Gas turbine engines are instrumental in the daily workings of our society. Used in many applications, including power plants, aircraft, and ships, gas turbines provide an efficient method of producing large amounts of power. Gas turbines are lightweight and quick to start up and shut down compared to older steam engines that are used in many power plants and ships. They have a high power-to-weight ratio and are relatively small, making them especially ideal for aircraft. Gas turbine engines consist of three main components: a compressor, a combustor, and a turbine.

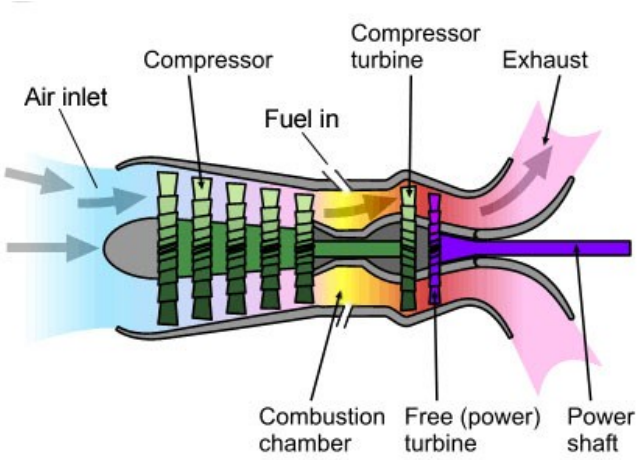

Figure 1: Basic gas turbine engine schematic [1].

Figure 1 displays a basic gas turbine engine schematic. Air enters the engine and first moves through the compressor. The compressor consists of numerous sets of sequentially smaller blades that compress the air, increasing its pressure and temperature. The air then proceeds to the combustion chamber where fuel is added to the compressed air and ignited. Ignition of the fuel releases energy in the form of heat into the compressed air, causing it to expand rapidly. This hot gas moves through the turbine, which consists of many sets of sequentially larger blades. The turbine blades are spun by the energized gas, producing power in the form of shaft power, thrust,

or a combination of the two.

The efficiency of a heat engine is defined as the ratio of the power output of the engine over the heat input. This heat input is provided by the fuel that is combusted. Extensive research has been completed on improving turbine efficiency to produce more power per unit of fuel, decreasing the cost of operation. An effective way to do this is by increasing the temperature of the gas flowing through the turbine. The hotter gas carries more of the fuel's energy through the turbine, which converts it into usable power. The problem is that as the temperature is increased to raise efficiency, the temperature of the gas will eventually exceed the melting temperature of the turbine blades and cause catastrophic failure of the turbine engine. A common way of mitigating this issue is by utilizing a process called "film cooling." Film cooled blades are hollow and have small holes drilled through the exterior of the blades.

Figure 2: Gas turbine blade with coolant holes in surface [2].

Figure 2 displays a photo of a gas turbine blade with coolant holes along its surface. Cooler air is diverted from the compressor when the gas turbine engine is running and pushed inside the hollow turbine blades and through the small holes. The objective of film cooling is to have the cooler air

coat the turbine blade and protect it from the hot air travelling from the combustor.

Film cooling is effective, but comes with its downsides. Current gas turbines divert as much as 30% of the air from the compressor for use in film cooling. That is a large amount of air that is being compressed, but is not traveling through the combustor to produce power. If the amount of air used for film cooling can be decreased, the engine efficiency will rise even more. Research has been conducted on the optimal location of the coolant holes, number of coolant holes in each blade, size of the holes, spacing of the holes, amount of air pushed through the holes, shape of the holes, etc. Despite this research, there is much that is unknown about film cooling, and engineers have not been able to produce a complete model of this process. The goal of this study is to produce data that can be used to make a more accurate model of the film cooling flows. This model can then be used to optimize the film cooling process by using a minimal amount of bleed air to produce a uniform layer of cool air over the blades, preserving the turbine blades from the combustion heat, yet reducing the amount of diverted compressor air.

The effectiveness of the film cooling is highest when the cooling film is attached across the surface of the turbine blade. This results in the most protection between the turbine blade and the hot gases. This is difficult to achieve because of a multitude of factors. The hot air coming from the combustor is turbulent and full of eddies and vortices. The pressure differential on either side of the turbine blades allows them to produce power, however, it also produces vortices that interfere with the flow on the other blades. The pressure differentials can also cause the cooling jets to detach from the blade surface sooner than typical. These factors make effective film cooling difficult to achieve without blowing an excess of cool air into the turbine.

Previous Work

There are many factors that determine the effectiveness of the cooling, and a variety of parameters that can be adjusted to achieve higher effectiveness. The curvature of the blades, pressure gradient effects, and freestream turbulence effects all affect film cooling. Freestream turbulence is the turbulence in the main flow exiting the combustor and flowing over the blades. The adjustable parameters include coolant hole configuration, hole shape, hole angle, and hole orientation. Numerous studies have been conducted to understand the effects of the different phenomena and parameters. This study will be focusing on the effect of pressure gradients on film cooling performance.

The performance of film cooling is represented by a nondimensional term called the film cooling effectiveness. Film cooling effectiveness is defined by Equation 1, where η is the film cooling effectiveness, T_∞ is the freestream, or mainflow, temperature, T_{aw} is the adiabatic wall temperature, and $T_{c,exit}$ is the temperature of the coolant at the coolant hole exit [3]. Adiabatic wall temperature in this case is the temperature the wall would have if there was no net heat transfer in or out of the surface. In this case it would equal the temperature of the fluid immediately above the turbine blade surface.

$$\eta = \frac{T_\infty - T_{aw}}{T_\infty - T_{c,exit}} \tag{1}$$

Blowing ratio (*M*), defined by Bogard and Thole [3], is the ratio of the coolant mass flux to the freestream airflow mass flux and is show in Equation 2, where ρ is the fluid density and u is the fluid velocity.

$$M = \frac{(\rho u)_c}{(\rho u)_\infty} \tag{2}$$

The momentum flux ratio (I) is defined as the ratio of the momentum of the coolant jet stream to the momentum of the freestream flow and is similar to the blowing ratio, but the coolant and freestream velocities are squared. It is also the scaling parameter for jet separation, meaning that if experiments are conducted at different scales, then I must be equal between the two scales to accurately analyze coolant jet separation.

Pressure gradient effects are present along different regions of the turbine blade due to its curvature. The curvature of the turbine blade causes the freestream flow and the flow of the film cooling jets to accelerate and decelerate, affecting the resulting film effectiveness. Figure 3 displays the regions of acceleration and deceleration in red and blue, respectively, as they occur over the surface of the turbine blade.

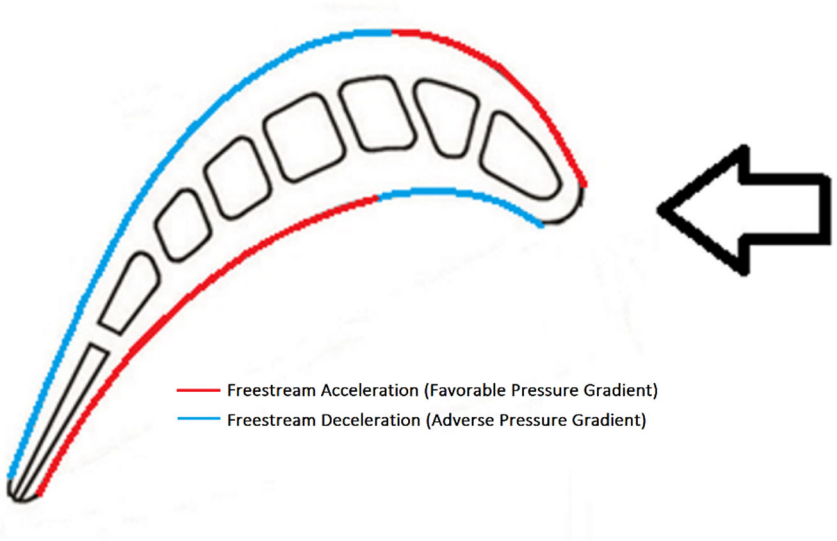

Figure 3: Cross Section schematic of a turbine blade to show areas of freestream acceleration and deceleration.

The direction and magnitude of the acceleration is dependent on the pressure gradient, whether it is adverse (negative acceleration parameter), or favorable (positive acceleration parameter). The acceleration along a turbine blade is described by the non-dimensional acceleration parameter (K). K is calculated using Equation 3, where v is kinematic viscosity, U_∞ is streamwise freestream

velocity, x is the distance downstream of the coolant holes, ρ is air density, and P is pressure. A positive x is downstream of the holes while a negative x is upstream of the coolant holes.

$$K = \left(\frac{\nu}{U_\infty^2}\right)\frac{\mathrm{d}U_\infty}{\mathrm{d}x} = -\left(\frac{\nu/\rho}{U_\infty^3}\right)\frac{dP}{dx} \tag{3}$$

The pressure gradient is favorable when K is positive and adverse when K is negative. There have been contradictory results observed for film cooling subject to different pressure gradients. For example, Teekaram et al. [4] found that a favorable pressure gradient of $K = 2.6\times10^{-6}$ increased film effectiveness whereas an adverse pressure gradient of $K = -2.6\times10^{-6}$ decreased film effectiveness. Brown and Saluja [5] on the other hand found that a favorable pressure gradient of $K = 1.1\times10^{-6}$ decreased film effectiveness significantly compared to an adverse pressure gradient of $K = -0.85\times10^{-6}$, which increased film effectiveness significantly. Bogard and Thole [3] reasoned that these different results might be due to different experimental conditions.

Lutum et al. [6] analyzed the effects of freestream acceleration on film cooling effectiveness over a convex surface with a favorable pressure gradient. The accelerated freestream flow experiment was conducted with an acceleration parameter K of 0.8×10^{-6}. It was found that generally the freestream acceleration caused the film effectiveness to decrease. This decrease in effectiveness was exacerbated as the freestream flow travelled along the streamwise direction of the blade. Figure 4 displays the comparison of the accelerated and constant velocity freestream flow conditions. As the streamwise distance increases the film effectiveness for the accelerated case decreases with respect to the zero acceleration case, supporting the above observation that film effectiveness with the accelerated freestream flow is decreased even further as streamwise distance increases. Although this study showed that freestream acceleration reduced film effectiveness on a convex surface, Lutum et al. [7] later found that freestream acceleration increased film

effectiveness on a concave surface.

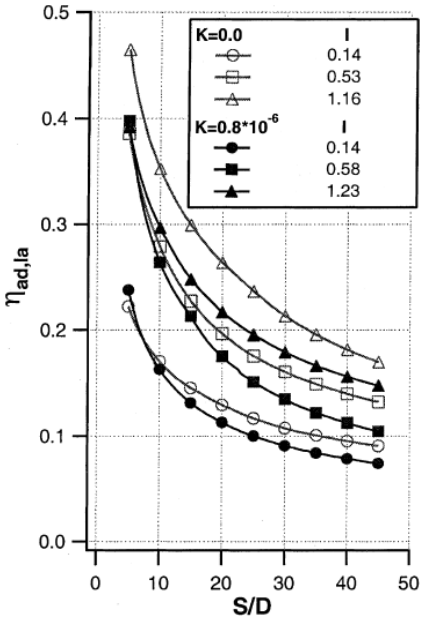

Figure 4: The film effectiveness of accelerated and constant freestream velocity flows as a function of streamwise distance, modified from Lutum et al [6].

Ryan et al. [8] tested film cooling under a variety of operation conditions, including comparing the jet stream tube and near wall concertation of cooling jets in zero, favorable, and adverse pressure gradients. The favorable pressure gradient had a K of 5.6×10^{-6} and the adverse pressure gradient had a K of -2.0×10^{-6}. Figure 5 shows the shape of the jet streamtube at a distance x = 15D downstream of the cooling hole where D is the cooling hole diameter. The coordinate y is the distance from the wall, and z is the spanwise coordinate perpendicular to x and y. The shape of the streamtubes is similar for the different pressure gradients, however, the concentration and distance off the blade surface varies. These data suggest that the jet in accelerating flow would be most effective at cooling the turbine blade because of its proximity to the blade. By this logic the jet would be least effective in decelerating flow due to its separation from the blade.

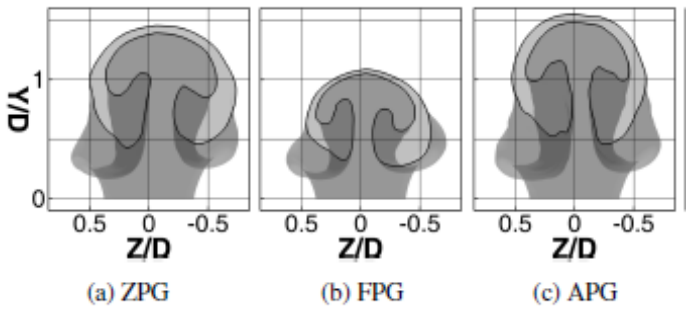

Figure 5: Cooling jet streamtubes in zero, favorable, and adverse pressure gradients. [8]

Figure 6 displays the near wall concentration of the coolant jets at a distance off the surface of $y = 0.15\text{D}$. The centerline concentration of the jet for the accelerating flow in the favorable pressure gradient is the greatest and it remains high for the longest streamwise distance. The decelerating flow has the lowest centerline concentration, but it has the greatest spanwise averaged concentration. The accelerating flow would have the best cooling effect the farthest from the coolant hole, but the decelerating flow would spread out and cool more blade area spanwise.

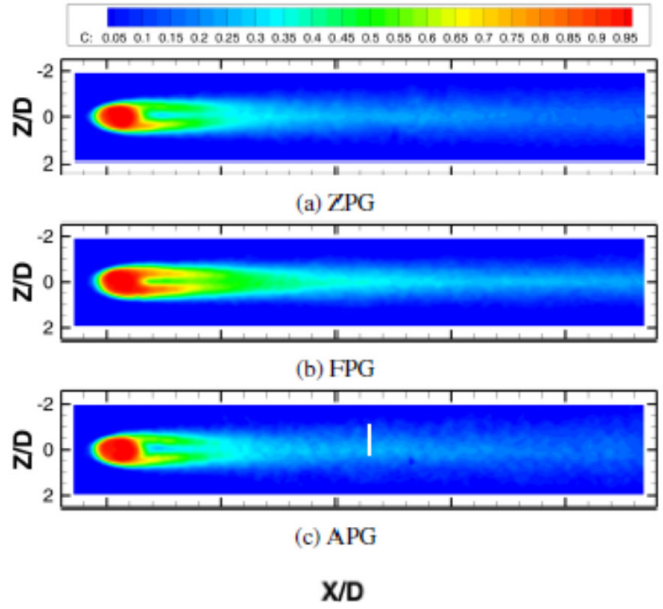

Figure 6: Near wall concentration of cooling jets in zero, favorable, and adverse pressure gradients. [8]

Maiteh and Jubran [9] analyzed the effect of pressure gradients on coolant flows with various coolant hole configurations and compound angles. The acceleration parameter in the experiment

ranged from -1.11×10^{-6} to 1.11×10^{-6}. Figure 7 displays the effect of pressure gradient on centerline film effectiveness at blowing ratios of 0.6 and 0.2. Maiteh and Jubran [9] concluded that a favorable pressure gradient reduces the film effectiveness due to the increased dilution of the coolant jet that takes place. An adverse pressure gradient increases the dilution of the coolant jets at greater magnitudes than the favorable pressure gradient at high blowing ratios, and thus reduces the film effectiveness by a greater amount. The effects of accelerating and especially decelerating flows is largely dependent on the blowing ratio.

Schmidt and Bogard [10] used a flat plate with a single row of round holes and a contoured top wall to create favorable and adverse pressure gradients across the cooling holes to measure their effect on film effectiveness. Their apparatus was similar to that of the present project. The acceleration parameter, K, ranged from 1.5×10^{-6} at the injection site to -0.5×10^{-6} 50 diameters downstream. For momentum flux ratios above 0.63, the film effectiveness was significantly less than at the lower momentum ratios. This can be attributed to the separation of the coolant jets at higher momentum flux ratios. For separated flow the pressure gradient did not have an effect on centerline film effectiveness. Fully detached flow does not effectively cool the gas turbine blades in any pressure gradient.

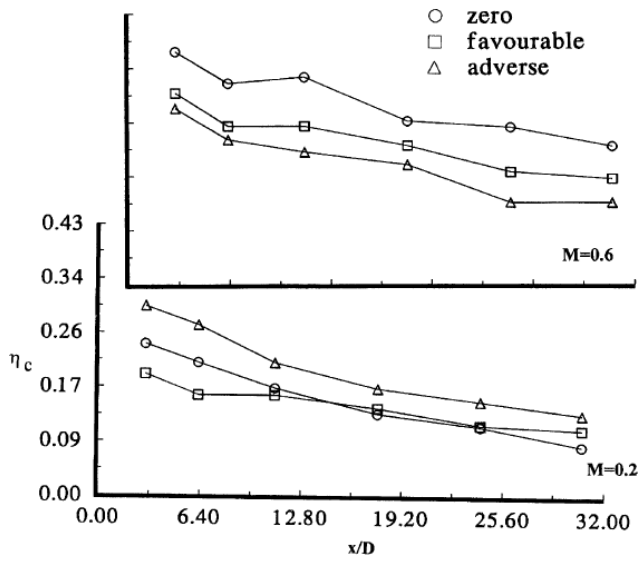

Figure 7: The effect of adverse, favorable, and zero pressure gradients on film cooling effectiveness [9].

Jessen et al. [11] used Particle-Image Velocimetry (PIV) to determine the velocity of the gas turbine blade boundary layer and coolant jet flows. Three offset rows of coolant holes were analyzed under zero and adverse pressure gradients. Under the zero pressure gradient condition the boundary layer velocity and turbulence were reduced close to the wall. Deceleration of the freestream flow caused the jet streams to lift up and penetrate deeper into the main flow. The adverse gradient increased the thickness of the boundary layer.

Project Purpose

There has been research into the effect of pressure gradients on film effectiveness, however, this research is not abundant and does not focus on freestream deceleration. This project studies the effect of an adverse pressure gradient in extensive detail by isolating this effect and testing a variety of experimental conditions. Rather than attempt to observe a wide variety of phenomena at a few conditions, the effects of freestream deceleration will be analyzed and compared at many conditions. The goal of this research is to understand the isolated effect of this specific phenomena.

This will serve as a building block for future studies and models related to gas turbine film cooling.

Experimentation

Experimental Theory

For the experiment to be scalable to a gas turbine engine, geometric and dynamic similitude must be satisfied. Geometric similitude consists of ensuring that the geometry of the experimental apparatus is scaled correctly to match the geometry of a gas turbine blade. The experimental apparatus used in this study is a flat plate, representing a small section of an actual turbine blade. This allows the effect of freestream deceleration to be isolated. The apparatus is scaled correctly, while keeping the coolant hole angle equivalent.

Dynamic similitude consists of running experiments under the same conditions seen within gas turbines. This requires making several non-dimensional parameters equivalent between a gas turbine engine and the experiment. This dimensional similitude allows the results of experiments and models to be applied to flows with different length and velocity scales. Two parameters that are matched are the Reynolds number and the Prandtl number. The Reynolds and Prandtl numbers are the scaling parameters for the velocity and thermal boundary layers. Matching these in the experimental conditions allows the heat transfer characteristics of the fluid flow to be analyzed and accurately scaled for use within gas turbines. These values allow for the prediction of velocity and thermal effects within the fluid flow and its surroundings. The Reynolds number is the ratio of the momentum forces and viscous forces within a fluid and is calculated using Equation 4, where D is the diameter of the coolant holes, U_∞ is the freestream velocity, and ν is the fluid kinematic viscosity.

$$Re_D = \frac{DU_\infty}{\nu} \tag{4}$$

Velocities are high within gas turbine engines. To achieve equivalence, the diameter of the holes in the experiment are larger than on a turbine blade to account for slower freestream velocities and differences in viscosities between the experimental gases and the gases within gas turbines. The freestream velocity is set at about 8 m/s to match the Reynolds number. The experimental Re_D is equal to 1×10^4, which matches the order of magnitude of typical Reynolds numbers found within gas turbine engines. The Prandtl number is the ratio of momentum diffusivity to thermal diffusivity and is calculated using Equation 5, where ν is the kinematic viscosity of the fluid and α is the thermal diffusivity of the fluid.

$$\mathrm{Pr} = \frac{\nu}{\alpha} \tag{5}$$

The Prandtl number within gas turbines is already close to equivalent to the Prandtl number in atmospheric air, so no consideration must be devoted to this parameter. The value of the Prandtl number in the experiment and within gas turbine engines is 0.7.

Blowing ratio (*M*) must also be matched for each testing condition. The temperature of the jets and the freestream flow in the experiment are 30 °C and 20 °C, respectively. Because of the low temperature difference between the two flows, any difference in the air density is negligible. This allows the densities in the blowing ratio equation to be cancelled, transforming *M* into a velocity ratio. Therefore, blowing ratio is controlled by changing the velocity of the coolant jets. Tests are run under three different blowing ratios, 0.5, 1.0, and 1.5, to determine the effect of freestream deceleration under different conditions. These blowing ratios have been used in previous studies and allow for experimental results to be compared at similar operating conditions. Another parameter that should be matched is the momentum flux ratio (*I*) between the freestream flow and

the coolant jets. This would require using fluids of two different densities for the freestream flow and jets. This parameter is not matched in these experiments because of the complexity it would require. Although important, matching the momentum flux ratio is secondary to matching the blowing ratio, so the results of the experiment are still useful even if the momentum flux ratios are not equivalent.

Finally, the acceleration parameter (K) is matched between the experimental apparatus and the operating conditions of a gas turbine engine. This parameter is controlled by modifying the geometry of the experimental apparatus for each condition. Like the blowing ratio, the acceleration parameter is changed throughout the testing to understand the effects of different magnitudes of freestream deceleration on film cooling. Three different acceleration parameters are tested, 0, -0.50×10^{-6}, and -0.68×10^{-6}.

There are five governing equations of fluid flow: the three Navier Stokes equations, the continuity equation, and the conservation of energy equation. The Navier-Stokes equations account for conservation of momentum in the x, y, and z directions; the continuity equation accounts for conservation of mass; and the conservation of energy equations account for conservation of energy. This yields five equations that have five unknowns: velocity in the three dimensions, temperature, and pressure. Solving these equations allows the properties of fluid flow to be determined at any point within a fluid flow. With five equations and five unknowns this system of equations has a solution. However, due to the nature of the equations they cannot be solved analytically. In theory they can be solved numerically using a process called Computational Fluid Dynamics (CFD). This process uses computers to iterate using finite element or finite difference

methods until a solution is found. To compute the exact solution, all features of the flow, including even the smallest turbulent fluctuations must be computed at all instants in time for the full flow under consideration. For the complicated conditions and geometries within a gas turbine this would require an enormous amount of time and computing power and is not practical for design purposes. Instead, experiments must be performed to understand the flow and create models that can be used to accurately simplify these equations. The simplified equations can be solved much more quickly, but include modeled terms. The accuracy of the solution depends on how well the modeled terms represent the behavior of the flow. One goal of experiments is to improve the understanding of the flow so that better models can eventually be developed. Matching the turbine geometry (geometric similitude) and the dimensionless parameters (dynamic similitude) in the experiment will yield equations that are equivalent for the model and the engine. In fact, the dimensionless parameters explained previously show up throughout these five governing equations. If the equations are equivalent, then the dimensionless solutions will be as well. The film cooling effectiveness and Stanton number, used to find the heat transfer coefficient and predict turbine blade temperature, are part of the dimensionless solution. Finding these values by measuring temperatures and velocities in the experiment gives solutions that are equal to those found in an actual turbine, given that the other dimensionless parameters listed previously are equivalent. This is what allows the experiment to be used to accurately predict the effects within gas turbines.

Experimental Methods

The primary deliverables of this research are the values of the Stanton number and film effectiveness at each condition. Knowing these two values at a certain set of non-dimensional parameters allows those values to be known under any conditions that match those same non-dimensional parameters. With these two parameters the convective heat transfer coefficient and

adiabatic wall temperature are found. These two values are used to calculate the surface temperature of the gas turbine blade. Being able to predict the temperature of the turbine blade is the ultimate goal in the real world because that is what determines if the turbine blades are going to fail due to the combustion gases being too hot. Film effectiveness is defined in Equation 1, and Stanton number is defined in Equation 6, where h is the convective heat transfer coefficient, ρ is the density of the freestream fluid, c_p is the specific heat of the fluid, and U_∞ is the freestream velocity.

$$St = \frac{h}{\rho c_p U_\infty} \tag{6}$$

The convective heat transfer coefficient is defined in Equation 7, where q''_{conv} is the convective heat flux flowing through the wall surface, T_s is the temperature of the wall, and T_{aw} is the adiabatic wall temperature.

$$h = \frac{q''_{conv}}{(T_s - T_{aw})} \tag{7}$$

As will be explained below, the test wall contains electric heaters, and temperature measurements are made with and without the test wall being heated. The convective heat flux, q''_{conv}, in Equation 7 is equal to the heat flux dissipated by the heating devices, which is found using the measured voltage and known resistance through the device, minus radiation and conduction losses, and divided by the surface area of each device. The specific heat, c_p, and density, ρ, of air are found in property tables. Substituting Equation 6 into Equation 7 and using this equation in combination with Equation 1 for both the heated and unheated cases results in four equations and four unknowns: Stanton number, film effectiveness, adiabatic wall temperature for the heated case, and adiabatic wall temperature for the unheated case. This system of equations is solved to find the Stanton number and film effectiveness at each experimental condition. These four equations are shown below, where St is the Stanton number, η is the film cooling effectiveness, q''_{heater} is the

heat flux provided by the heaters, $q"_{cond}$ is the heat flux lost through conduction out the back of the test wall, $q"_{rad}$ is the heat flux lost through radiation out the front of the test wall, T_s is the surface temperature of the test wall, T_∞ is the freestream temperature, $T_{c,exit}$ is the exit temperature of the coolant jets, and $T_{aw,h}$ is the adiabatic wall. The *h* and *u* subscripts denote that the variables were either measured with the wall heated or unheated, respectfully. The only unknowns in these equations are the Stanton number, the film cooling effectiveness, and the adiabatic temperatures for the heated and unheated cases.

$$St = \frac{q"_{heater} - q"_{cond,h} - q"_{rad,h}}{T_{s,h} - T_{aw,h}} \tag{8}$$

$$St = \frac{-(q"_{cond,u} + q"_{rad,u})}{T_{s,u} - T_{aw,u}} \tag{9}$$

$$\eta = \frac{T_{\infty,h} - T_{aw,h}}{T_{\infty,h} - T_{c,exit,h}} \tag{10}$$

$$\eta = \frac{T_{\infty,u} - T_{aw,u}}{T_{\infty,u} - T_{c,exit,u}} \tag{11}$$

Experimental Facility

Experiments are conducted in a low speed wind tunnel. Figure 8 displays a photo of the wind tunnel, including the test section. Air enters the wind tunnel from an upstream blower. The air velocity is set using a variable frequency drive that controls the blower speed. After exiting the blower, the air flow enters a diffuser that decreases its velocity. It then passes through a honeycomb which causes the air flow to become one dimensional, and a series of screens aimed to decrease the freestream turbulence in the flow. This one-dimensional, low turbulence air then enters a nozzle which accelerates the air and further decreases its turbulence. The flow then enters the test section where data are recorded.

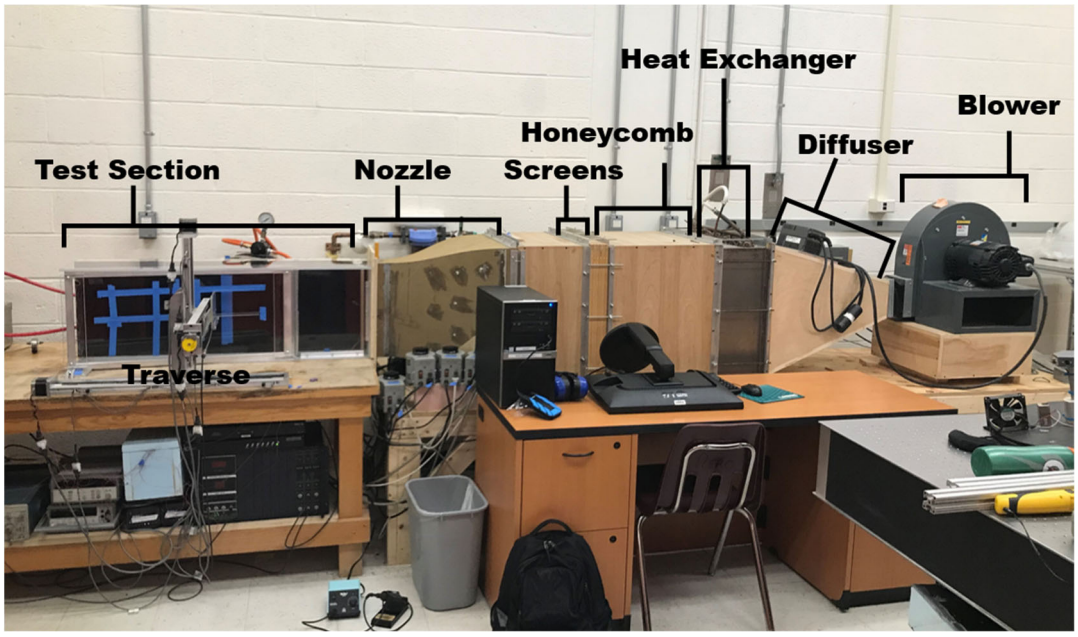

Figure 8: Labelled photo of the experimental apparatus.

The wind tunnel from the blower to the nozzle was first designed and constructed for the Trident project of Coulthard [15] and has subsequently been used with little modification in the Trident projects of Womack [12], Pelzer [13] and the present study. The test section was designed and constructed new for the present study.

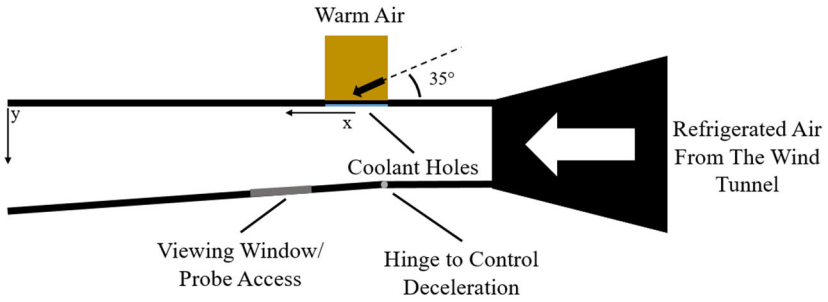

Figure 9: Schematic of the test section from a bird's eye view.

The test section includes two vertical walls which the flow moves between. Figure 9 displays a schematic of the test section. One of the walls is parallel to the flow exiting the nozzle. This wall is the test wall. The other wall is hinged so that it can be angled away from the test wall. This expansion creates a constant adverse pressure gradient and decelerates the freestream flow

uniformly. The hinge is located 15 cooling hole diameters upstream of the downstream edge of the cooling holes (x = -15D). The rate of deceleration is set by changing the angle of the flat plate across from the test surface. By increasing the angle, the magnitude of uniform deceleration increases. This angle cannot exceed approximately seven degrees because the airflow separates from the plate and the uniform deceleration of the desired magnitude is not obtained. The acceleration parameter values shown below in the testing matrix in Table 1 were chosen to be small enough to prevent this separation.

Table 1: Originally Proposed Experiment Testing Matrix.

Experiment	Acceleration Parameter (K)	Blowing Ratio (M)
1	0	0.5
2	0	1
3	0	1.5
4	-0.1×10^{-6}	0.5
5	-0.1×10^{-6}	1
6	-0.1×10^{-6}	1.5
7	-0.3×10^{-6}	0.5
8	-0.3×10^{-6}	1
9	-0.3×10^{-6}	1.5
10	-0.5×10^{-6}	0.5
11	-0.5×10^{-6}	1
12	-0.5×10^{-6}	1.5

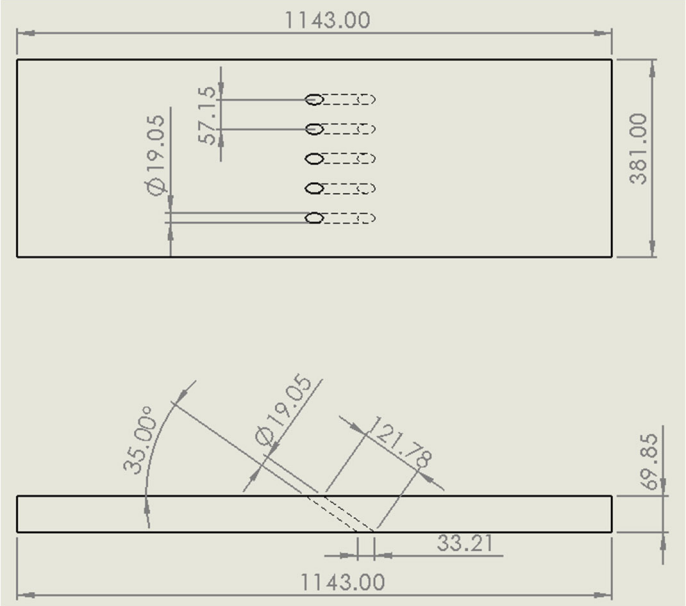

Figure 10: Test wall dimensions in millimeters.

The test wall is made of 69.85 mm thick high-density urethane foam surfaced with a 2 mm sheet of smooth PVC Komatex® foam. The test wall includes five cylindrical coolant holes, which were placed in a row, as shown in Figure 10. The diameter of the coolant holes is 19.05 mm. The spanwise distance between the five coolant holes is 3D, the length of the coolant holes through the foam wall is 6.4D, and they are angled 35 degrees incident to the test wall surface. These dimensions were chosen to provide geometric similarity to what is found in actual gas turbine engines. Thermocouples are placed to measure the temperature of the film coolant and the freestream flow. The angled wall is designed to include a removable insert that can be changed for different measurements. One insert includes a 196.85 × 508 mm infrared viewing window across from the cooling holes so the surface of the test wall can be observed with an IR camera. This insert is shown in Figure 11. This window consists of 0.019 mm thick polyolefin shrink wrap stretched over a frame and inserted into the removable window. This wrap is then heated to shrink the film and remove any wrinkles.

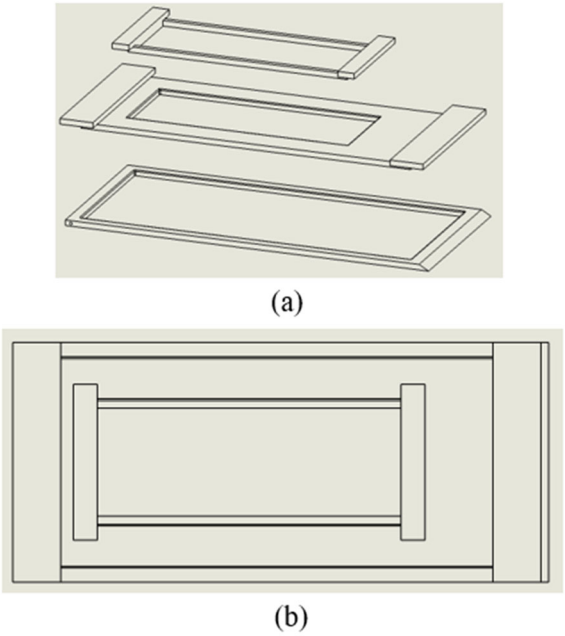

Figure 11: IR window (a) Exploded and (b) front views.

An infrared camera (described below) faces the test wall to record the temperature of the surface in the field of view provided by the window. The infrared viewing window in Figure 11 can be removed and replaced with a slotted acrylic window, shown in Figure 12, that allows probes to be inserted into the flow to measure temperature and velocity. The vertical slots are placed 2, 6, 10, and 18D downstream of the downstream edge of the coolant holes. The probes are held by a programmable traversing device that allows them to be moved to different locations in the flow.

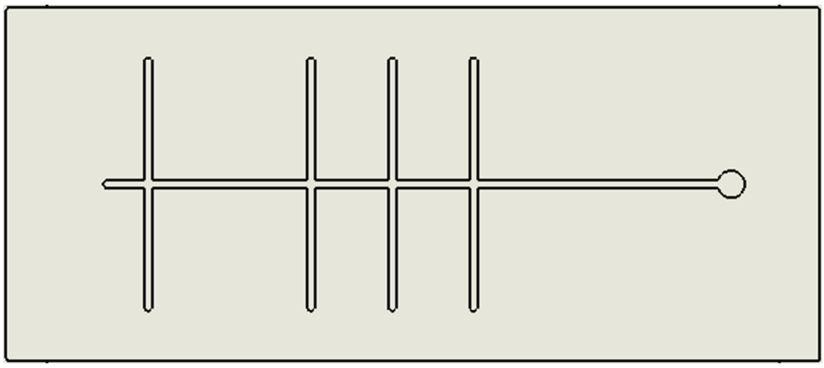

Figure 12: Slotted insert for data collection with probes.

The test wall includes four, thin heating elements, placed between the urethane foam and the

Komatex® surface sheet, and located upstream and downstream of the cooling holes to control the temperature of the surface. The heating elements are flexible, foil-etched Kapton heaters made by All Flex Inc. The heater dimensions are 254×279.4×0.229 mm and have a foil pattern shown in Figure 13. The nominal advertised resistance of each element is 13.092 ohms. The heating elements were placed under the Komatex® precisely to generate uniform heating over the surface. Air is supplied to the cooling holes from a plenum behind the test wall.

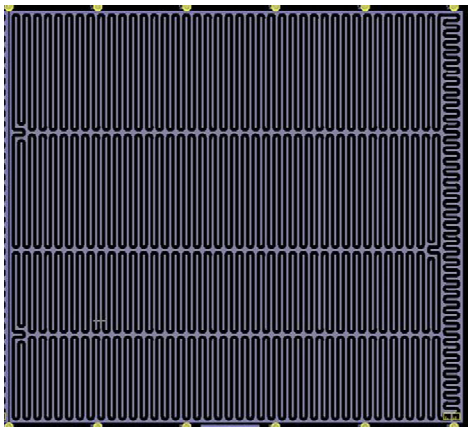

Figure 13: Etched foil pattern of the All Flex Inc. Kapton heating elements.

The plenum was reused from the previous Trident project [13], but modified. Figure 14 shows a labelled picture of the plenum attached to the test section. It was sealed to prevent air leakage, and the entrance holes for the pressurized air were enlarged to enable a greater flowrate out of the coolant holes. The coolant air enters the plenum from the pressurized air system within the building. It travels through a pressure regulator to control the flowrate of the air and then flows through nine 1.5mm diameter holes to enter the plenum. This causes the air to be choked going into the plenum so that the flow rate is not affected by any pressure changes downstream. After the air is inside the plenum, it travels through a heat exchanger and then through two mesh screens before exiting out of the coolant holes. Hot water from a hot water bath is pumped through the plenum heat exchangers at 30 °C to heat up the air. The purpose of the mesh screens is to even out

the pressure differential of the flow in the plenum to achieve equal coolant velocity out of each hole.

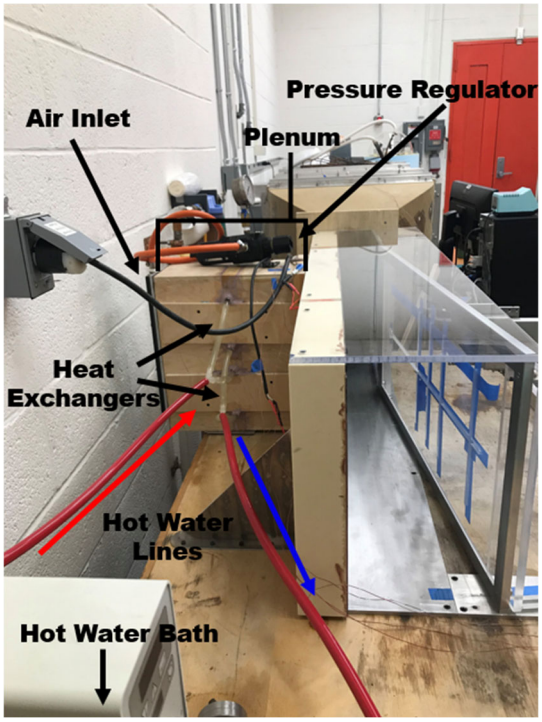

Figure 14: Labelled photo of the plenum.

The freestream air coming from the wind tunnel is cooled to 20 °C before it enters the apparatus, and the cooling holes are blowing air that is warmed to 30 °C. Although this is opposite of what happens in a gas turbine, the heat transfer characteristics will be equal, just in the opposite direction. Having the hot and cold fluids reversed has some effect on the density and viscosity of the air, which is the opposite of the engine, but keeping the temperature difference small prevents these differences from being significant.

Experimental Measurements

Temperature data are collected using thermocouples and an infrared (IR) camera. Thermocouples are used to measure the freestream temperature, coolant jet exit temperature, room temperature,

and back test wall surface temperature. Hot wire velocity probes and particle image velocimetry (PIV) are used to conduct velocity measurements. Hot wire velocity probes are used to set the freestream velocity, blowing ratio, and acceleration parameter for each condition. They are also used for taking velocity and turbulence profiles. Thermocouples are temperature measuring devices that consist of two wires of different materials that are welded together at a junction. Temperature differences between the two ends of the wires create a voltage that can be measured and converted into temperature. E-type thermocouples are used in this study. The thermocouples are soldered together at one end to create the dissimilar metal junction. These wires are then led into an insulated box where each is soldered to a copper wire. The junctions between the thermocouple wires and copper wires are electrically insulated and sandwiched between two aluminum plates. The metal plates within the insulated box serve as a thermal mass that keep all the junction points at the same temperature. The copper wires are then led out of the insulated box and into the voltage measuring equipment. Two thermocouples are placed vertically in an ice bath at two different depths. The ice bath allows the measured voltages from the other thermocouples to be compared to a reference voltage for which the temperature is known, and the different depths allow the two reference thermocouples to be compared. If these reference thermocouples begin to read different values, then they are at different temperatures which is indicative of the ice melting. The conversion from the thermocouple voltages to temperatures is performed using calibration coefficients from the National Institute of Standards and Technology (NIST) for E-type thermocouples.

The infrared camera (FLIR SC8300 HD) is used to measure the surface temperature of the test wall. The camera detects infrared waves given off by surfaces. These infrared waves are produced

by heat energy and can be measured and converted into temperatures across the surface that the camera is facing. The camera is set up about two meters from test wall to get the picture focused. It looks at the test wall through the infrared window described above. The emissivity and transparency of the window and Komatex® test wall surface are measured and used to correct the thermal counts given off by the camera to the correct temperature. The camera is calibrated before each set of images using a blackbody source to ensure the accurate collection of data. The software provided with the camera can be set to provide a reading in raw counts at each pixel in the field of view or a temperature at each pixel computed from the count value. The raw measured counts are taken from the camera and temperatures are computed outside the IR camera software using Matlab code written as part of the present project. This allows for better accounting of radiation absorbed and reflected by the test wall and IR window. The IR camera is angled slightly, about seven degrees, from normal to the test wall so that its reflection cannot be seen in the IR window. This slight distortion of the field of view caused by this angle was corrected so that the distance between the measured points on the test wall is accurate. This was correction was performed by comparing a known distance, the diameter of the coolant holes, with the number of pixels that span that distance in the IR picture. Using this method, the pixels were converted into distances.

Hot wire velocity probes consist of a thin wire suspended between two prongs. Electricity is run through this wire so that it heats up. The visible wire is one resistor in a Wheatstone bridge that makes up the hot wire probe. As the air flows across the wire it cools the wire. The voltage is automatically adjusted using an anemometer to counteract the cooling and maintain the wire at a constant temperature. The voltage needed to maintain the wire's temperature is proportional to the velocity of the air. The anemometers used in this research are an A. A. Lab Systems AN-1003 Test

Module and a TSI IFA 300. The first anemometer was used to collect data for the $K = 0$ and $K = -0.5\times10^{-6}$ cases, but became inoperable due to a broken switch, so the second anemometer was used for the remainder of the data collection. The hot wire probes are calibrated every four weeks using a venturi and a manometer.

Particle image velocimetry (PIV) is a method of measuring instantaneous velocity in a flow. The flow is seeded with a tracer, in this case fog created from olive oil, and then illuminated to make the tracer particles visible. The seed was fed into the wind tunnel through the blower. The illumination comes from a laser sheet that lights up all the particles in a single plane. A camera is set up perpendicular to the laser sheet. The velocity of the flow is calculated using software that determines the difference in position between each tracer particle in two images taken a short and know time interval apart (200 μs in the present measurements). This yields a velocity field representation of the flow. A 200 mJ pulsed YAG Big Sky Laser is used with a TSI 8 mega pixel camera. The camera is used with a Nikon, 105 mm micro-lens.

Uncertainty Analysis

An uncertainty analysis was performed for the thermocouples, hot wire velocity probe, IR camera, and heater output flux. The analysis focused on random error. Bias errors in the calculated heat flux would not affect the Stanton number ratios because they would cancel out in the ratio. The expanded uncertainty for each measurement was estimated based off observations and data taken throughout the study. The sensitivities of each measurement on Stanton number and film cooling effectiveness were calculated using the following method. The temperature values from the thermocouples were changed by a known amount, and then the Stanton number and film cooling

effectives were calculated. The amount that the two parameters had changed with respect to their original values was recorded and divided by the amount the temperature was changed. This was repeated for the IR camera temperatures, freestream velocity, and heat flux. Each sensitivity was multiplied by its respective expanded uncertainty and the product was squared. These values were summed for the Stanton number with jets, Stanton number without jets, and film cooling effectiveness, and then the square root of the sum was taken to determine the uncertainty for each parameter. The relative uncertainty for the two Stanton numbers are combined using the root mean square method to find the relative uncertainty for the Stanton number ratio. This relative uncertainty is multiplied by the Stanton number ratio to get an absolute uncertainty. The Stanton number, film cooling effectiveness, and Stanton number ratio have uncertainties, of +/- 6.5×10^{-4}, +/- 0.048, and +/- 0.31, respectively.

Experimental Conditions

The original proposed experimental testing matrix is shown above in Table 1. Four acceleration parameters were to be tested. The first condition tested was a control at an acceleration parameter of 0. This case had a constant velocity freestream flow. The next three acceleration parameters had varying strengths of an adverse pressure gradient, and therefore varying magnitudes of freestream deceleration. Three blowing ratios were to be tested at each acceleration parameter, and the film effectiveness and heat transfer coefficient calculated at each experimental condition. After evaluating the Stanton number and film effectiveness for the $K = 0$ and $K= -0.5\times10^{-6}$ conditions the test matrix was revised and is shown in Table 2. The $K = -0.5\times10^{-6}$ had a small effect on the Stanton number and film effectiveness, so the experiment was modified to test stronger magnitudes of deceleration. The final test matrix is shown in Table 3. It was determined that strongest

magnitude of deceleration that could be tested was $K = -0.68\times10^{-6}$ because any more deceleration would result in separation of the freestream flow from the test wall. Separation would render the results unusable because it is not a representation of what occurs inside a gas turbine engine.

Table 2: Revised Testing Matrix

Experiment	Acceleration Parameter (K)	Blowing Ratio (M)
1	0	0.5
2	0	1
3	0	1.5
4	$-0.5\text{x}10^{-6}$	0.5
5	$-0.5\text{x}10^{-6}$	1
6	$-0.5\text{x}10^{-6}$	1.5
7	$-0.75\text{x}10^{-6}$	0.5
8	$-0.75\text{x}10^{-6}$	1
9	$-0.75\text{x}10^{-6}$	1.5
10	$-1.0\text{x}10^{-6}$	0.5
11	$-1.0\text{x}10^{-6}$	1
12	$-1.0\text{x}10^{-6}$	1.5

Table 3: Final Testing Matrix

Experiment	Acceleration Parameter (K)	Blowing Ratio (M)
1	0	0.5
2	0	1
3	0	1.5
4	$-0.5\text{x}10^{-6}$	0.5
5	$-0.5\text{x}10^{-6}$	1
6	$-0.5\text{x}10^{-6}$	1.5
7	$-0.68\text{x}10^{-6}$	0.5
8	$-0.68\text{x}10^{-6}$	1
9	$-0.68\text{x}10^{-6}$	1.5

For each testing condition the apparatus is started up and given time for all the conditions to become steady. This takes roughly one and a half hours for each experimental condition. Thermocouples are used to verify that the temperatures of the freestream flow and coolant flows are correct and hot wire velocity probes are used to ensure their velocities are correct. The desired

acceleration parameter is used to determine the angle at which the apparatus wall will be set. Care must be taken to check for flow separation on any of the four walls of the test section, because if the angle is too great, causing the separation of airflow from the surface, the experimental findings will be inaccurate. To find film cooling effectiveness and Stanton numbers, surface temperature data are collected with the heating elements on and off. The IR camera is used to measure the temperature distribution on the test wall. Thermocouples are used to measure the freestream temperature, T_∞, the jet temperature, $T_{c,exit}$, and the ambient air temperature. The power supplied to the heater is recorded. From these measurements, the film cooling effectiveness and Stanton number are determined at all locations on the test wall.

To help understand and explain the effect of deceleration on film effectiveness and Stanton number, additional measurements are also taken. A thermocouple probe is inserted into the flow, followed by a hot-wire velocity probe, to find the temperatures and velocities at different points within the flow. Measurements such as temperature, velocity, and turbulence profiles, as well as temperature grids of the jet cross sections at different downstream distances yield an understanding of the fluid and jet characteristics at those points. The traverse is programmed to move the probes and collect data automatically. These measurements are followed by Particle Image Velocimetry (PIV). Olive oil mist is seeded into the flow and a camera is used to collect velocity data in the plane normal to the freestream flow at x = 10D. This gives a survey of the cross section of the jets. These velocity fields are useful for explaining why the heat transfer effects are occurring because they show where the coolants jets are going, how they are spreading out, and how far they are from the surface.

Expected Results

It can be concluded by observing the results of previous experiments involving pressure gradients in film cooling that favorable pressure gradients typically result in slightly lower film effectiveness levels when compared to film cooling in a zero pressure gradient. Adverse pressure gradients tend to produce slightly greater effectiveness at low blowing ratios, however at higher blowing ratios, coolant flows in adverse pressure gradients produce film effectiveness even less than those produced in favorable pressure gradients. The studies previously conducted that measured the effect of an adverse pressure gradient used a single acceleration parameter and focused solely on the film cooling effectiveness. This study will measure the effects of an adverse pressure gradient over a range of acceleration parameters, and will determine the heat transfer coefficient at each condition.

Results

Wind Tunnel Uniformity

Before beginning the experimental testing matrix, a number of tests were performed to ensure that the wind tunnel was producing uniform flow and that the measurement devices were measuring accurately. In the first test, temperature and velocity grids were taken at the outlet of the wind tunnel nozzle. This ensures that the temperature and velocity are uniform, and that the freestream turbulence is as low as expected. Figure 15 (a) shows the temperature grid taken. Points were taken in a 13 by 4 square grid with a distance of 1.33D between each point. The temperature is uniform across the grid and is close to the 20 °C set point of the chiller water cooling the wind tunnel heat exchanger. It increases slightly towards the left side because the probe is moving into the thermal boundary layer of the test wall, which is at ambient temperature. The ambient air temperature in

the room where the grid was taken is slightly above the freestream temperature.

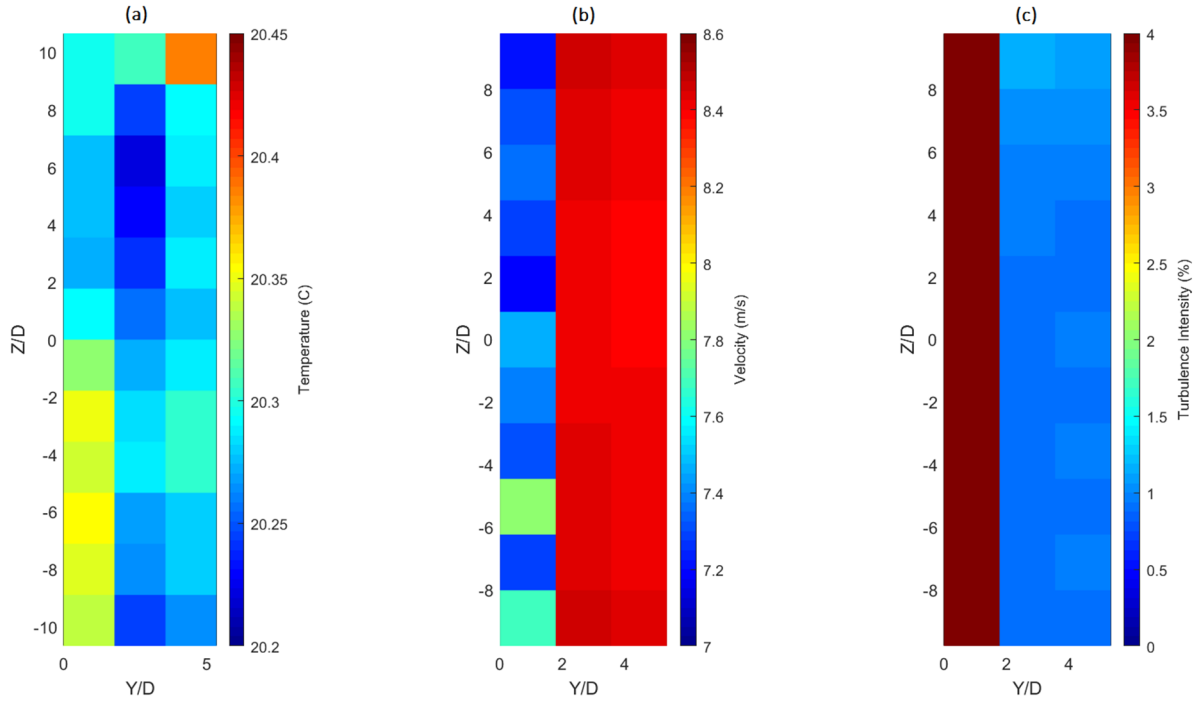

Figure 15: The (a) temperature, (b) velocity, and (c) turbulence intensity fields at the outlet of the wind tunnel nozzle.

Figure 15 (b) displays the velocity grid taken. Like the temperature grid, the velocity grid appears uniform and all velocities are within 0.41% of the average freestream velocity, 8.4 m/s. The velocity decreases slightly towards the test wall because the probe is beginning to move into the boundary layer. The temperatures and velocities in the grids are uniform and are behaving as expected. Figure 15 (c) shows the turbulence intensity grid. Turbulence intensity is the ratio of the root mean square of the velocity fluctuations, taken over a time period, to the mean velocity over that same time period, and is presented as a percentage of the mean freestream velocity. This figure shows the component of turbulence in the streamwise direction. The turbulence intensity is uniform away from the wall, but increases as the probe gets close to the wall. This is expected because the probe enters the boundary layer, which is more turbulent. The freestream turbulence is low and uniform, at 0.96% +/- 0.09% in the center of the nozzle, meaning that the honeycombs

and screens within the wind tunnel apparatus are working well. Most of the readings away from the wall are below 1% turbulence.

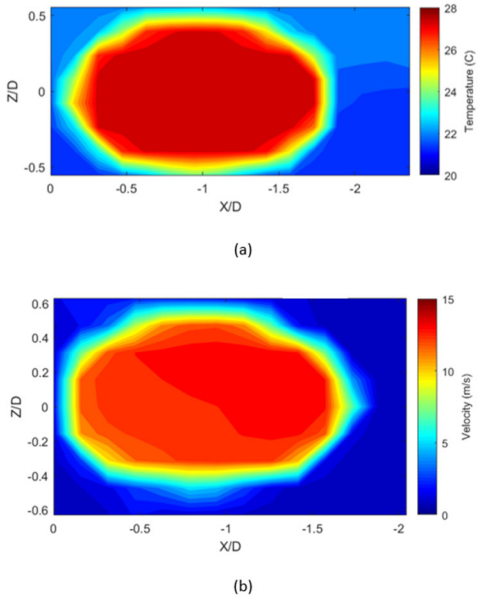

Figure 16: Coolant hole outlet (a) temperature and (b) velocity surveys.

Temperature and velocity grids were taken at the exit of the center coolant hole to ensure that the flow temperatures and velocities are symmetric around the axis of the jet. Figure 16 (a) displays the temperature grid at the exit of the middle coolant hole. It appears as expected. The coolant jet is heated to 30 °C in the plenum, and the center of the plot shows temperature just under 28 °C. As the probe moves out of the center of the jet the temperature drops to the ambient air temperature of 21 °C. The hole grid is not circular because the coolant hole angle causes the hole to appear elliptical as it intersects the test wall surface. Figure 16 (b) shows what appears to be a similar grid to (a), however it is a velocity grid. The coolant jet is set to a velocity of 12 m/s, which would correspond to a blowing ratio of 1.5 if the freestream air were flowing. The center of the grid shows velocities of 12 m/s, that decrease to 0 m/s as the probe moves out of the jet and into the still air.

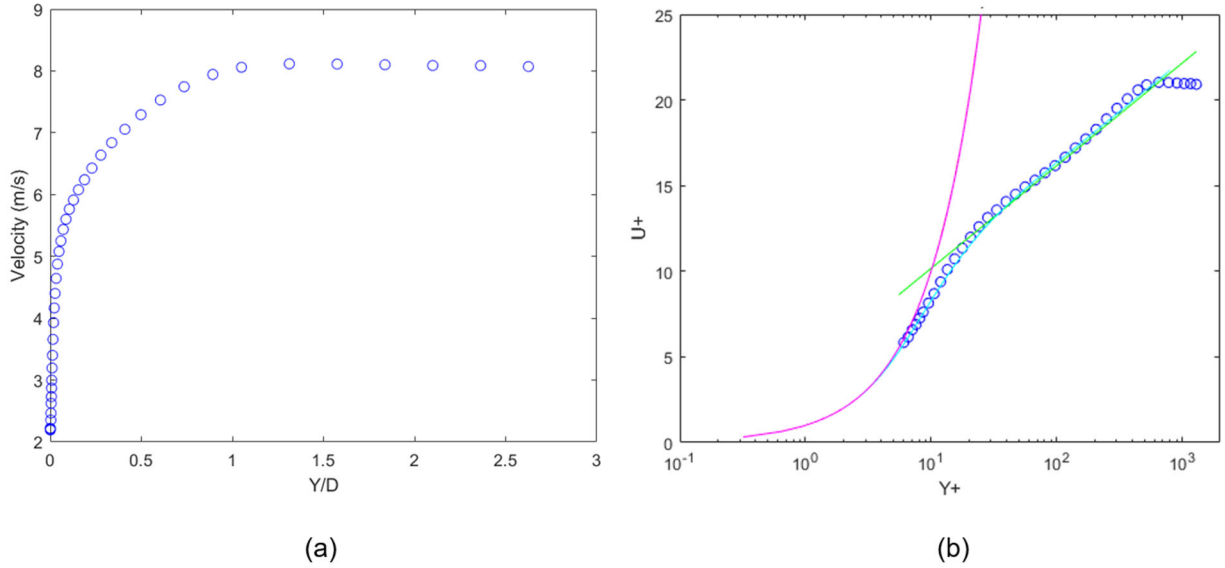

Figure 17: Velocity profiles for K = 0 on a (a) linear and (b) log scale with the Law of the Wall, upstream (x = -3.22D) of the coolant holes.

The outer wall of the test section was set to produce $K = 0$, and measurements were made without the jets. Temperature and velocity profiles were taken with and without the wall heaters, respectively, and an IR picture of the test wall surface was taken. The coordinate system origin was set at the downstream edge of the center cooling hole. The temperature, velocity, and turbulence profiles were taken at an upstream location, $z = 0$ and $x = -3.22D$, and a downstream location, $z = 0$ and $x = 12D$. The upstream velocity profile, shown in Figure 17 is plotted on a logarithmic scale using wall coordinates, shown in Figure 17 (b) and analyzed using the Law of the Wall. The velocity profile goes from approaching 0 m/s close to the wall, to leveling out at 8 m/s, the freestream velocity. Wall coordinates are a non-dimensional method of representing the distance from the wall and the velocity using the skin friction coefficient and fluid properties. The coordinate $y^+ = \frac{(y+y_o)U_\infty\sqrt{C_f/2}}{\nu}$, where C_f is the skin friction coefficient and y_o is the wall offset. The wall offset is a correction for the actual location of the first measurement point in the profile.

The coordinate $U^+ = \frac{U}{\left(U_\infty\sqrt{\frac{C_f}{2}}\right)}$, where U is the local mean velocity. The Law of the wall consists of two separate lines, shown above in pink and green, that model the velocity profile of a turbulent boundary layer. A single line that matches these two curves and fits the region between them using Van Driest damping, as explained in Kays and Crawford [14], is shown in light blue. The skin friction coefficient and y offset from the wall were iterated until the experimental profile fit the Van Driest equation. From there the skin friction coefficient, boundary layer thickness, momentum thickness, and momentum Reynolds number were extracted. These K = 0 profiles were used to verify that the wind tunnel was producing boundary layer and thermal boundary layer characteristics that were expected. Later, during the freestream deceleration cases, velocity, turbulence, and temperature profiles were collected at all three acceleration parameters without the coolant jets, and velocity and turbulence profiles were collected at the downstream location for all nine experimental conditions with the coolant jets. The boundary layer characteristics for all cases without jets are shown in Table 4.

Table 4: Flow characteristics from velocity profiles.

Acceleration Parameter	Downstream Coordinate	Skin Friction Coefficient	Boundary Layer Thickness (mm)	Momentum Thickness (mm)	Momentum Thickness Reynolds Number
0	-3.22D	4.55×10^{-3}	19.0	1.96	1.06×10^{3}
0	12D	4.15×10^{-3}	24.2	2.65	1.44×10^{3}
-0.50×10^{-6}	-3.22D	3.85×10^{-3}	21.2	2.46	1.32×10^{3}
-0.50×10^{-6}	12D	3.30×10^{-3}	28.6	3.70	1.82×10^{3}
-0.68×10^{-6}	-3.22D	3.70×10^{-3}	20.6	2.59	1.35×10^{3}
-0.68×10^{-6}	12D	3.05×10^{-3}	30.8	4.30	1.95×10^{3}

Figure 18 shows the upstream temperature profile and fits it with the thermal law of the wall. This is a similar concept to that shown in Figure 17 (b), but as it applies to the thermal boundary layer. The pink and green lines are the thermal Law of the Wall model, that model the temperature profile of the thermal boundary layer. The coordinate $T^+ = \frac{(T_0 - T)U_\infty\sqrt{C_f/2}}{\dot{q}"_0/\rho c}$ where T is the local mean

temperature, T_0 is the wall temperature, $\dot{q}"_0$ is the convective heat flux through the wall, τ_0 is the shear stress at the wall, and ρ and c are the density and specific heat of the air at its film temperature.

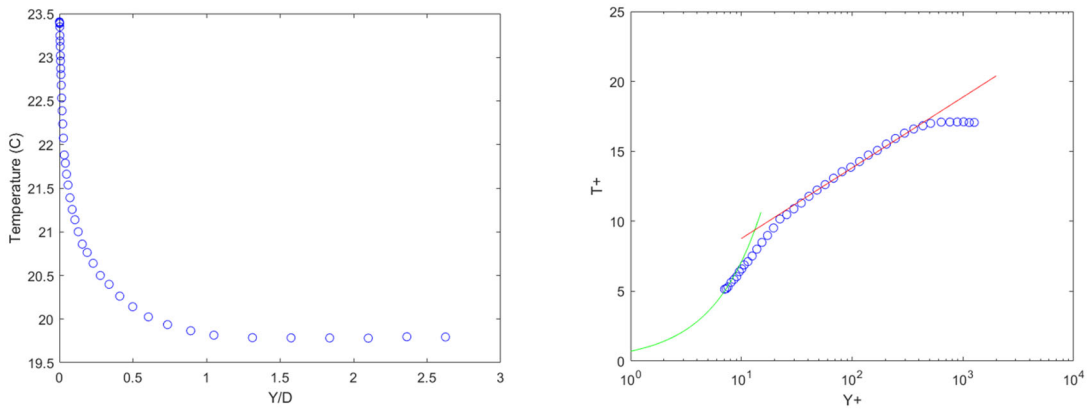

Figure 18: Temperature profiles for K = 0 on a (a) linear and (b) log scale with the Law of the Wall, upstream (x = -3.22) of the coolant holes.

The temperature profile was taken with the wall heated and goes from just under 20 °C in the freestream, to approaching the surface temperature of the wall. Fitting the experimental data to the thermal law of the wall allows the wall temperature, thermal boundary layer thickness, enthalpy thickness, enthalpy thickness Reynolds number, and Stanton number to be calculated. The thermal boundary layer characteristics for all cases are shown in Table 5.

Table 5: Thermal flow characteristics from temperature profiles.

Acceleration Parameter	Downstream Coordinate	Wall Temperature (°C)	Thermal Boundary Layer Thickness (mm)	Enthalpy Thickness (mm)	Enthalpy Thickness Reynolds Number	Stanton Number
0	-3.22D	24.95	18.8	1.61	0.85×10^{3}	2.8×10^{-3}
0	12D	25.20	28.7	3.16	1.68×10^{3}	2.3×10^{-3}
-0.50×10^{-6}	-3.22D	25.75	19.2	1.54	0.81×10^{3}	2.6×10^{-3}
-0.50×10^{-6}	12D	25.47	29.1	3.06	1.50×10^{3}	2.3×10^{-3}
-0.68×10^{-6}	-3.22D	25.37	20.3	1.75	0.90×10^{3}	2.5×10^{-3}
-0.68×10^{-6}	12D	25.75	29.9	3.36	1.51×10^{3}	2.3×10^{-3}

Using the IR camera data, the Stanton number was calculated for each point across the test wall. The spanwise average of the Stanton number across the middle three hole pitches (-4.5D<z<4.5D)

is calculated and plotted against the downstream distance in Figure 19. The Stanton number is calculated theoretically under the same conditions and also plotted.

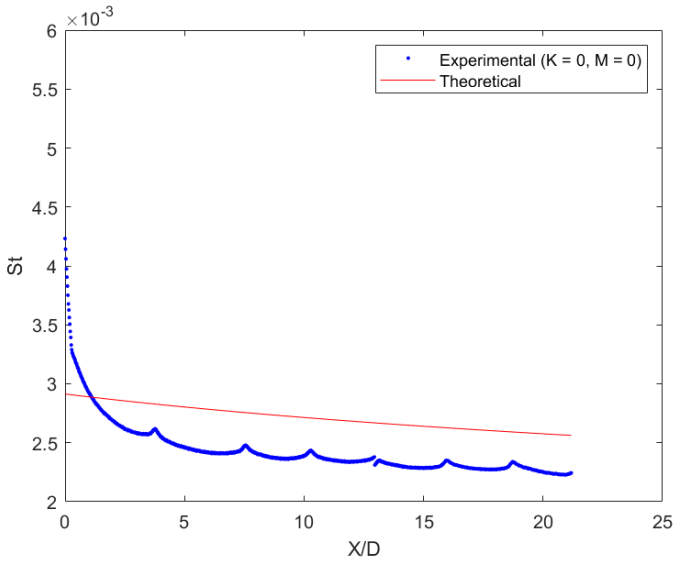

Figure 19: Experimental and theoretical Stanton number comparison.

The theoretical and experimental curves do not match well until x = 4.5D. This is because the gap in the heaters as the air flows over the coolant holes is not taken into account in the theoretical calculations. This gap causes the actual Stanton number to increase significantly because the thermal boundary layer becomes thin and must rebuild. From x = 4.5D to x = 22D the two curves have an average difference of 13.3%. This difference is believed to be a bias error due to inaccuracies when measuring the heater resistance. This does not influence the analysis because the Stanton number ratios between cases with and without film cooling are compared, and the difference in the Stanton numbers cancel out because the bias error is the same for each case.

Comparison to Previous Studies

After the test section conditions were measured and compared to correlations from the literature, data were taken under similar conditions to previous work to ensure that the present results are

reproducing results that have already been observed. Figure 20 compares the centerline and spanwise averaged film effectiveness taken at K = 0 to data taken by Coulthard et al. [15] under the same conditions. The data taken in this study do not agree exactly with the data taken by Coulthard et al., however they follow the same trend for each of the conditions. The differences seen between the present data and the Coulthard et al. data are of the same magnitude as the differences between Coulthard et al. and other studies. The differences between the data sets fall within the uncertainty range for this study, except for the M = 1.5 case. The average differences in the centerline film effectiveness between the two data sets for each blowing ratio are 0.05, 0.02, and 0.09, respectively. The average differences in the spanwise averaged effectiveness are 0.01, 0.02, and 0.09, respectively. For both centerline and spanwise averaged film effectiveness, the M = 1.5 case shows the greatest difference in results between this study and Coulthard et al.

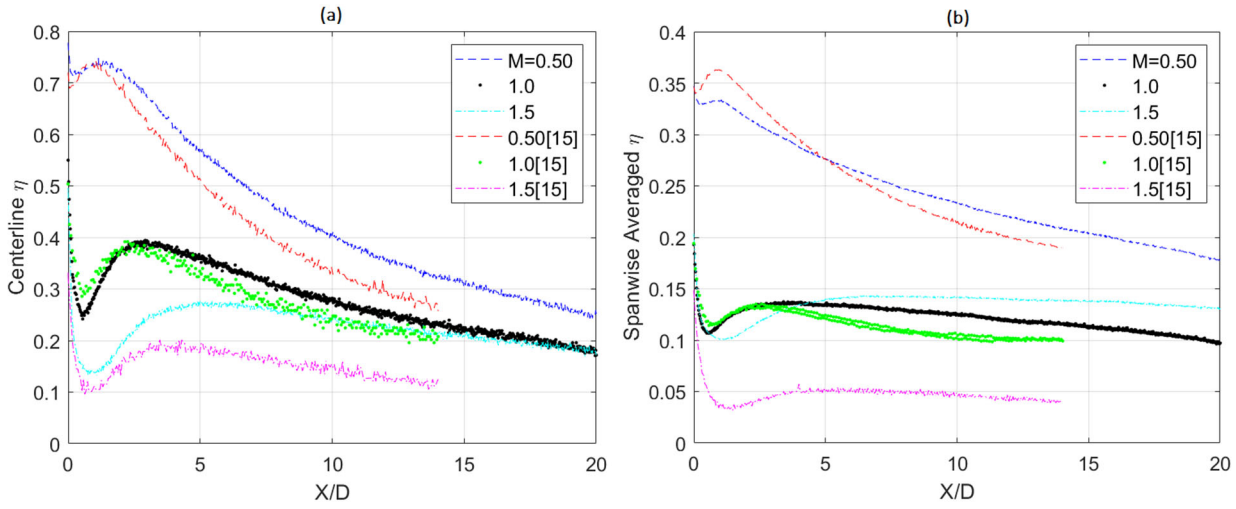

Figure 20: (a) Centerline and (b) Spanwise averaged film effectiveness comparison at K = 0 [15].

The Stanton number ratio is defined as the ratio of the Stanton number with the jets on to the Stanton number without the jets blowing. Stanton number results were also compared to the results of Coulthard et al. [16] with K = 0 and various blowing ratios. Figure 21 displays the comparison between the two data sets. The data taken in this study match with the Coulthard et al. data and

follow the same trends and all cases fall within the Stanton number ratio uncertainty range. The average difference in the centerline Stanton ratio between the two data sets for each blowing ratio is 0.1, 0.05, and 0.01, respectively. The average difference in the spanwise averaged ratio is 0.1, 0.02, and 0.01, respectively. The greatest difference in Stanton number ratios between this study and Coulthard et al. occurs in the M = 0.5 case.

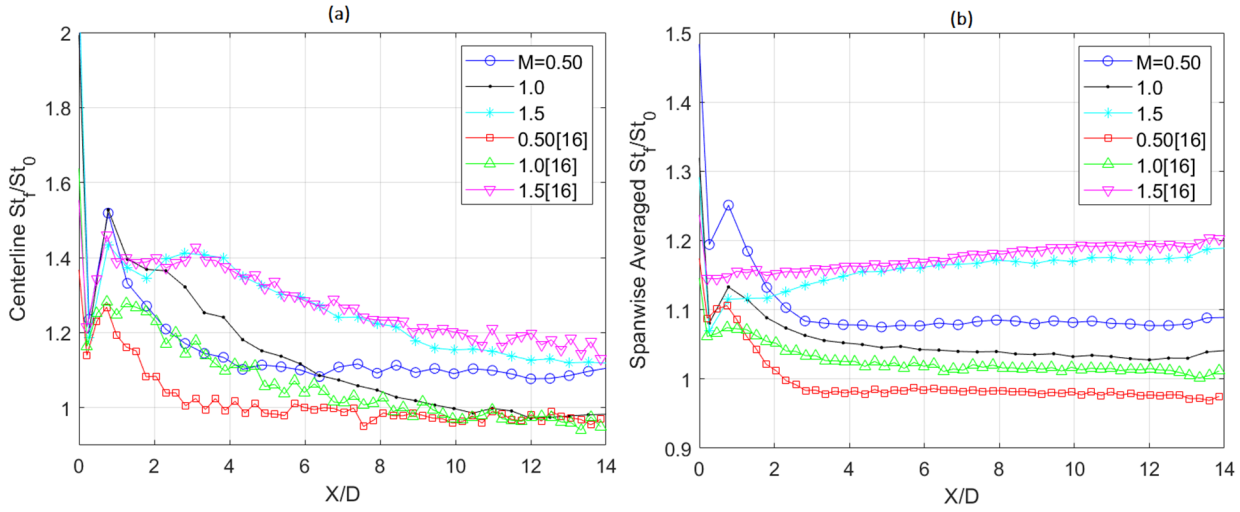

Figure 21: (a) Centerline and (b) Spanwise averaged Stanton number ratio comparison at K = 0 [16].

Freestream Deceleration Cases

To increase the effectiveness of film cooling there are two metrics, film cooling effectiveness and Stanton number. The film cooling effectiveness compares the wall's adiabatic temperature to the coolant jet temperature, and a higher film cooling effectiveness means that the film cooling is more effective. The Stanton number measures how much heat transfer is occurring between the surface and the freestream flow, so a lower Stanton number is preferred because it means that there is less heat transfer into the turbine blade. As mentioned before, the first set of data were taken at an experimental condition of $K = 0$ to compare and verify the results found at that acceleration parameter to previous studies. These data also serve as a control to which the data taken at varying

acceleration parameters can be compared. This allows the effect of the pressure gradient on film cooling to be established. The first set of non-control data was taken at an acceleration parameter of -0.50×10^{-6}. Figure 22 shows the centerline and spanwise averaged film effectiveness at $K = 0$, $K = -0.50\times10^{-6}$, and $K = -0.680\times10^{-6}$ across all three experimental blowing ratios. The centerline film effectiveness graph shows that as the blowing ratio increases, the film effectiveness decreases. For the $K = 0$ cases the film effectiveness peaks at 0.73, 0.39, and 0.27 for $M = 0.5$, 1.0, and 1.5, respectively. As the blowing ratio increases the peak effectiveness occurs further downstream of the coolant holes, occurring at x = 1.3, 2.3, and 5.9D, for the respective blowing ratios. The film effectiveness at each blowing ratio converges toward the same value as the downstream distance increases. The $K = -0.50\times10^{-6}$ case decreases the film effectiveness by about 3% at a blowing ratio of 0.5 at its peak value. It remains 0.04 lower than the $K = 0$ case as the jets travel downstream. The $K = -0.68\times10^{-6}$ case decreases the film effectiveness by about 11% at a blowing ratio of 1.5 at its peak value. It remains 0.02 lower than the $K = 0$ case as the jets travels downstream. The adverse pressure gradient has little effect on the film effectiveness in the $M = 0.5$ and $M = 1.0$ cases and this effect is the greatest when the downstream distance is least. The freestream deceleration has the greatest effect on centerline film effectiveness when $M = 1.5$. The film effectiveness is, on average, 0.03 less than the $K = 0$ case, at $K = -0.50\times10^{-6}$ and 0.07 less at $K = -0.68\times10^{-6}$. The higher blowing ratio coolant jet has a higher likelihood of separating from the surface, and the adverse pressure gradient in the freestream deceleration cases has a greater effect on pulling the jets off the wall, decreasing the film effectiveness. The differences between these cases fall within the uncertainty range with a few exceptions. The difference is significant for the $M = 1.0$ cases from downstream distance 0D to 4.85D, and for the $M = 1.5$ cases. As downstream distance increases the film effectiveness across the different blowing ratios converge.

The spanwise averaged film effectiveness plot shows a similar trend for the M = 1.5 case, where the K = -0.5×10^{-6} pressure gradient decreases film effectiveness by 20% at the peak value. The freestream deceleration cases for M = 0.5 and 1.0 begin at a similar film effectiveness as the control, but as X/D increases, effectiveness diverges for all cases at these blowing ratios. At M = 1.5 both deceleration cases decrease spanwise averaged film effectiveness, with the K = -0.68×10^{-6} case resulting in a greater decrease as seen in the centerline film cooling effectiveness as well. The different blowing ratio cases converge as downstream distance increases, but at a lesser rate than for the centerline film effectiveness. The only significant difference in spanwise averaged film cooling effectiveness occurs for the M = 1.5 case from a downstream distance of 0D to 18D. The M = 1.0 and 1.5 film cooling effectiveness are not significantly different. The only significant effect of freestream deceleration on film cooling effectiveness occurs when the blowing ratio is equal to 1.5, and this effect is quite small.

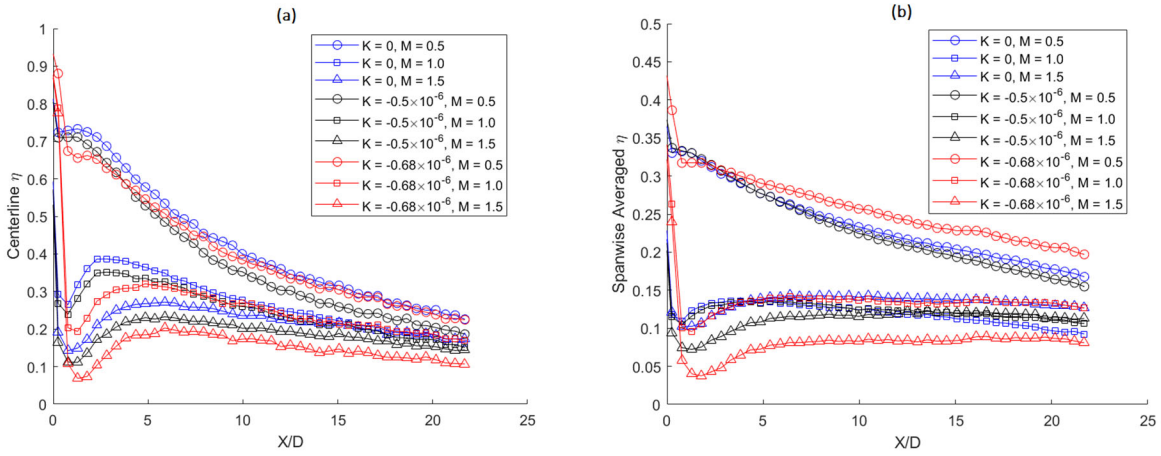

Figure 22: (a) Centerline and (b) spanwise averaged film effectiveness for all acceleration parameters.

Figure 23 shows contour plots of the film effectiveness at each condition. These plots allow the results seen in Figure 22 to be visualized and explained. The film cooling effectiveness in the M = 0.5 cases is much greater than in the M = 1.0 and 1.5 cases. That is most likely due to the

increased velocity causing the coolant jet to separate from the surface of wall for the higher blowing ratio cases. There are no visible differences between the decelerated cases and the zero acceleration case when M = 0.5 and 1.0. At M = 1.5 the centerline and spanwise film cooling effectiveness decrease slightly as the magnitude of deceleration increases. The pattern in the K = 0 contour plots show similar patterns to contour plots taken at K = 0 in the Coulthard et al. research.

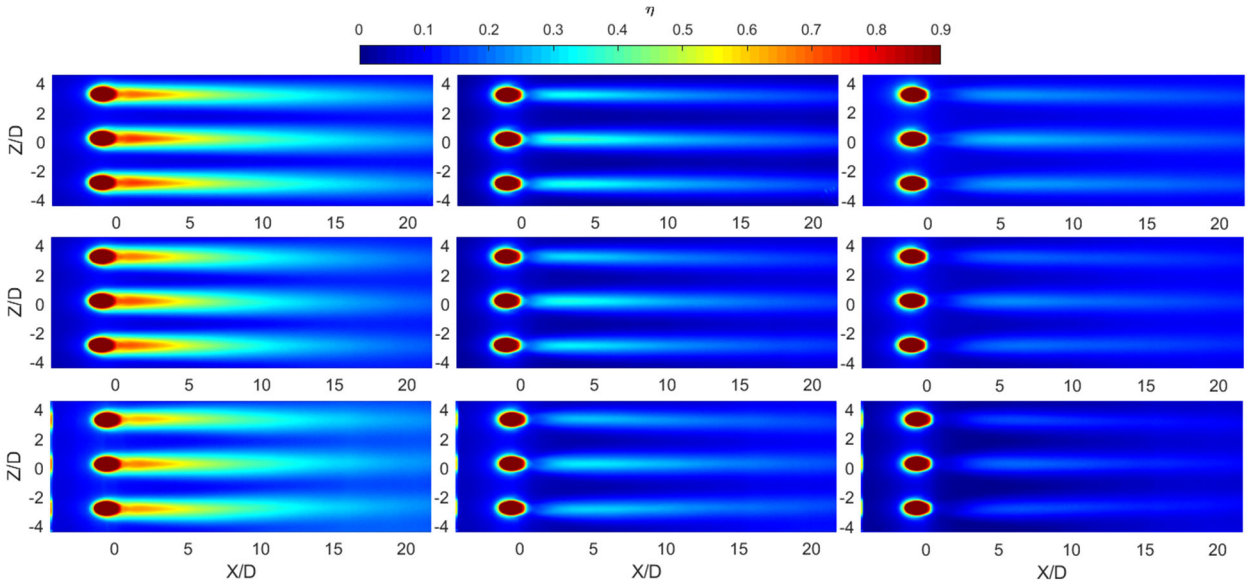

Figure 23: Film effectiveness contour plots under the following conditions: from left to right M = 0.5, 1.0, and 1.5, and from top to bottom K = 0, -0.5×10^{-6}, -0.68×10^{-6}.

Figure 24 shows the centerline and spanwise averaged Stanton number ratios for each condition studied. For the K = -0.50×10^{-6} case, the centerline Stanton number ratios increase as the blowing ratios increase. This is expected, as the higher velocity coolant jets cause a higher coefficient of heat transfer, leading to a larger Stanton number. For the K = 0 and K = -0.68×10^{-6} cases, this same trend holds, with the exception that the M = 0.5 cases have a larger centerline Stanton number ratio than the M = 1.0 case. All cases show a decrease in Stanton number ratio as downstream distance increases. The decelerated M = 1.5 cases have greater spanwise averaged Stanton number

ratios than the zero acceleration case. An interesting note is that at the downstream distance of 22 D, the spanwise average Stanton number ratios are greater than the centerline ratios at that same distance. The spanwise average ratios decrease less rapidly than the centerline ratios as X/D increased, with the spanwise averaged $M = 1.5$ cases increasing with downstream distance. These differences all fall within the uncertainty range for the Stanton number ratio and therefore freestream deceleration has no significant effect on Stanton number ratio.

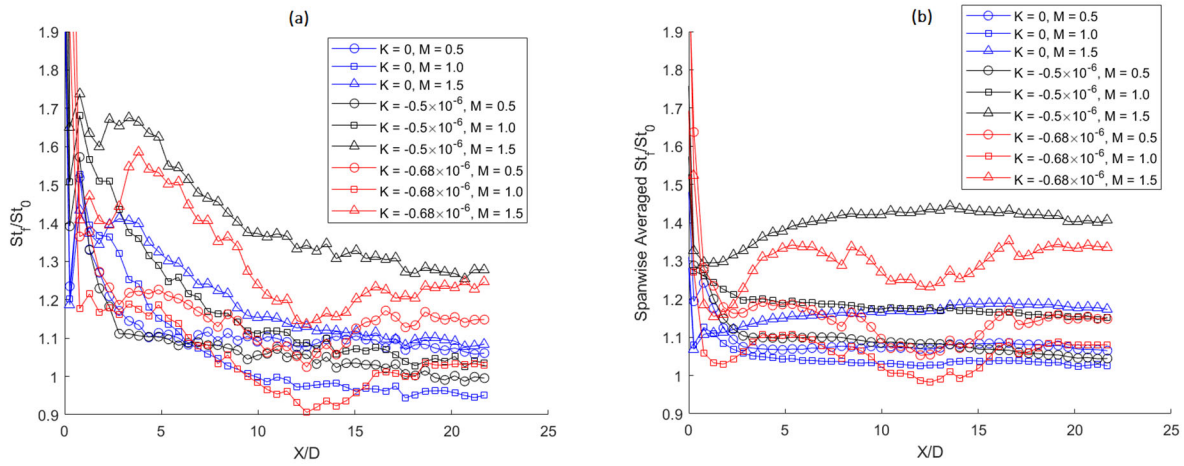

Figure 24: (a) Centerline and (b) spanwise averaged Stanton number ratios for all cases.

Figure 25 is a contour plot comparison of the Stanton number ratios at each experimental condition. In all the plots a V-shape in the Stanton number ratio is observed downstream of each coolant hole. Previous studies have shown that the coolant jets contain two counterrotating vortices, shown in Figure 5, that cause the coolant stream to touch down on the surface to the sides of the jet centerline and pull away from the surface at the centerline. This explains why the centerline Stanton number ratios are lower than the spanwise averaged ratios at increasing downstream distances. The centerline Stanton number ratios for all cases decrease significantly as the jet moves downstream because the vortices move away from the centerline. This V-shaped pattern has been observed in other film cooling research, including Coulthard et al. [16]. As the blowing ratio increases the coolant jets cause the V-shape to appear further downstream, at x = 2, 7, and 8 D for the blowing

ratios of M = 0.5, 1.0, and 1.5, respectively. As the blowing ratio increases so does the tendency for the coolant jet to lift off. The higher blowing ratios cause the jets to lift off sooner. Further downstream the vortices either become larger or move closer and make contact with the wall. This explains why the V-shape occurs further downstream for higher blowing ratios. For the M = 0.5 cases, the Stanton number ratio contour plot is similar for the $K = -0.50\times10^{-6}$ and zero acceleration cases. These ratios are greatest in the $K = -0.68\times10^{-6}$ case. The Stanton number ratio increases from the K = 0 to the $K = -0.50\times10^{-6}$ cases when M = 1.0 and 1.5. For the M = 1.5 cases the V-pattern downstream of each hole join with the V pattern of the adjacent hole at x = 14D for the K = 0 case, and x = 10D for the $K = -0.50\times10^{-6}$ and $K = -0.68\times10^{-6}$ case. There is much more noise in the $K = -0.68\times10^{-6}$ case than in the two other acceleration parameter cases, both in Figure 24 and 24. Although there are visible differences between the cases with different acceleration parameters, these are not significant.

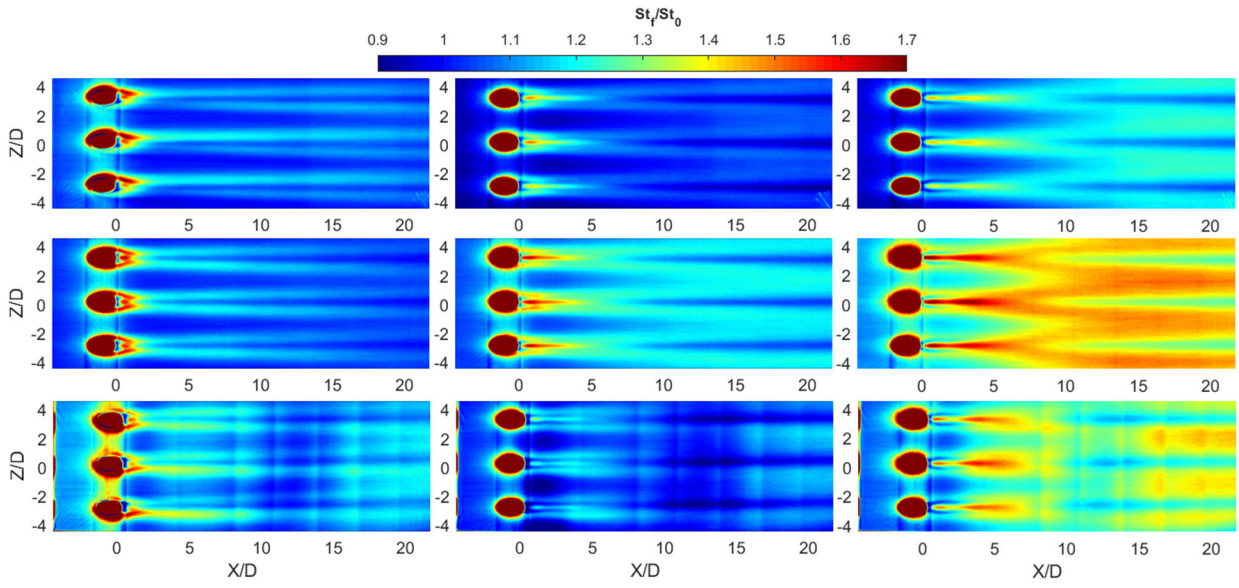

Figure 25: Stanton number ratio contour plots under the following conditions: from left to right M = 0.5, 1.0, and 1.5, and from top to bottom K = 0, -0.5×10⁻⁶, -0.68×10⁻⁶.

Freestream deceleration, at the magnitudes studied, has little to no effect on film cooling

effectiveness and Stanton number ratio. This is useful information because it adds another piece of understanding to the study of film cooling. The absence of an effect allows models to be simplified because cases of freestream deceleration can be approximated as zero acceleration cases.

Additional Flow Measurements

Equation 12 defines θ, where T is the temperature of the flow at a point, T_∞ is the freestream temperature, and T_{jet} is the coolant jet temperature. θ is a non-dimensional representation of temperature.

$$\theta = \frac{T - T_\infty}{T_{jet} - T_\infty} \tag{12}$$

Figures 25, 26 and 27 display a temperature cross section of the center coolant jet in terms of θ at downstream distances of 2D, 10D and 18D, for all cases. As seen in Figure 26, as the blowing ratio increases the jet begins to separate away from the wall. For the M = 0.5 case the jet is concentrated close to the wall at a high θ. As blowing ratio increases, the θ of the jets decrease as well as their concentration near the wall. Beginning when M = 1.0 and more noticeable when M = 1.5, two lobes form in the coolant jets. These are the counter rotating vortices that pull the jet away from the wall on the jet centerline and force the jet back towards the wall on the outside. The freestream deceleration decreases θ and pulls the jet away from the wall slightly at x = 2D when compared to the zero acceleration case, but it doesn't have much of an effect in Figure 26. This behavior is expected, and helps explain why film effectiveness generally decreases and Stanton number generally increases, as blowing ratio increases.

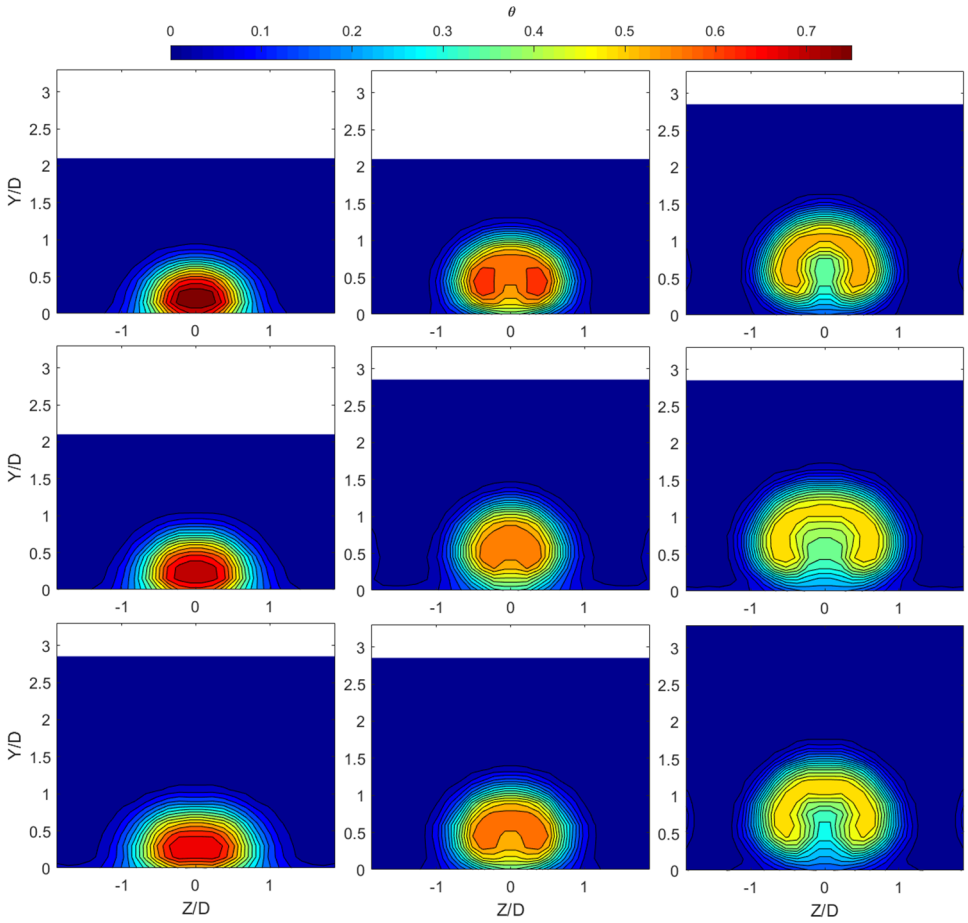

Figure 26: Coolant jet temperature cross sections at x = 2D, in θ temperature units, under the following conditions: from left to right M = 0.5, 1.0, and 1.5, and from top to bottom K = 0, -0.5×10^{-6}, -0.68×10^{-6}.

Figure 27 shows temperature cross sections at x = 10D. Most noticeable is the great decrease in θ between the downstream distance of 2D in Figure 26 and 10D shown in Figure 27. As the coolant jet moves downstream and mixes with the freestream flow, θ decreases dramatically. The jets spread out as the downstream distance increases and the two lobes seen in Figure 26 are not clearly visible. For the $M = 0.5$ case the jets remain close to the wall like they were when x = 2D, however, the jets at the other blowing ratios begin to pull away from the wall as compared to Figure 26. The freestream deceleration cases stretch the jets away from the wall, however, this is a small effect. θ is greater in the $M = 1.0$ cases than in the other cases. This suggests that when the jet and freestream velocities are equal, the jet temperature stays concentrated for longer. The edges of the adjacent

jets begin to appear in the cross section frames as the jets spread out with increased downstream distance, blowing ratio, and deceleration magnitude.

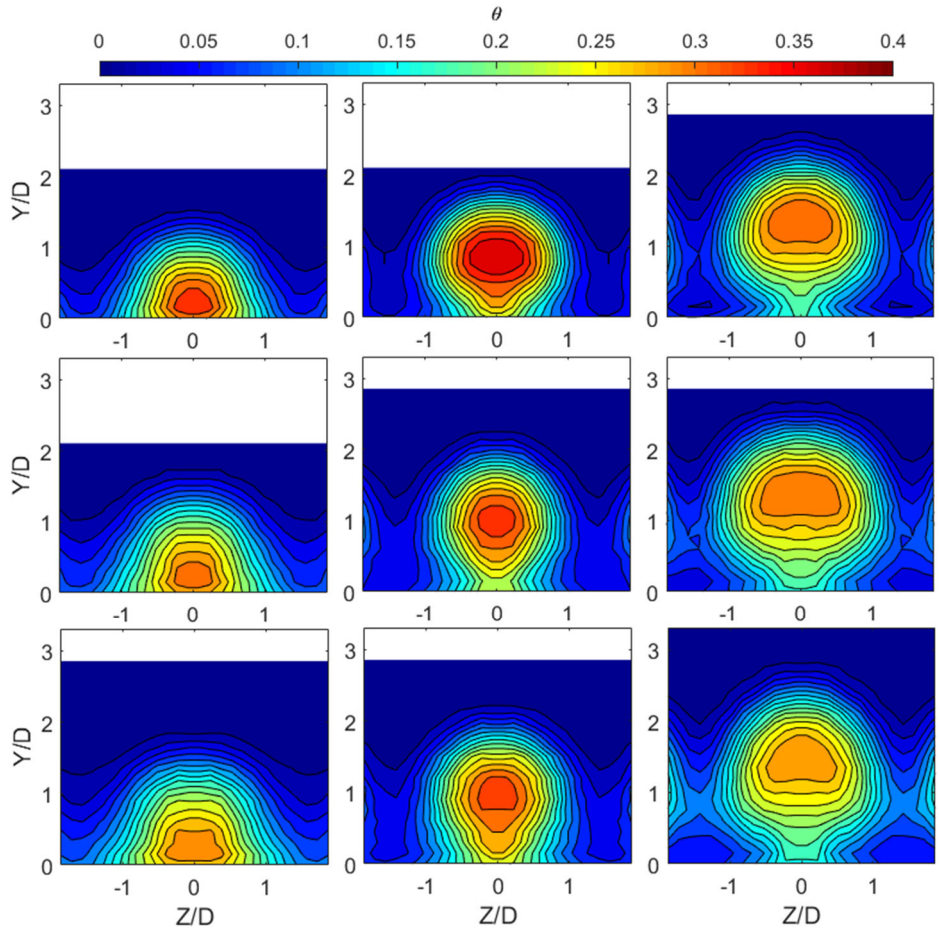

Figure 27: Coolant jet temperature cross sections at x = 10D in, θ temperature units, under the following conditions: from left to right M = 0.5, 1.0, and 1.5, and from top to bottom K = 0, -0.5×10^{-6}, -0.68×10^{-6}.

Figure 28 shows the coolant jet temperature cross sections at x = 18D. The θ in these cross sections are less than in the x = 10D cross sections, but not by much. After that initial decrease between x = 2D and 10D, the θ value remains steadier as downstream distance increases. The M = 0.5 cases remain close to the wall, with the M = 1.5 cases being noticeably separated from the wall. The effect of deceleration is not as evident at this downstream distance. The deceleration spreads the jet out along the wall, explaining the increased Stanton number ratios at higher deceleration

magnitudes and downstream distances. The decelerated cases at $M = 1.0$ are thinly stretched. That stretched look is not as noticeable in the other decelerated cases.

These temperature surveys support previous results showing that freestream deceleration has little effect on the behavior of the flow. Overall, the behavior of the coolant jets in these surveys is expected and consistent with the behavior of the film effectiveness and Stanton number seen from the IR camera experimental method.

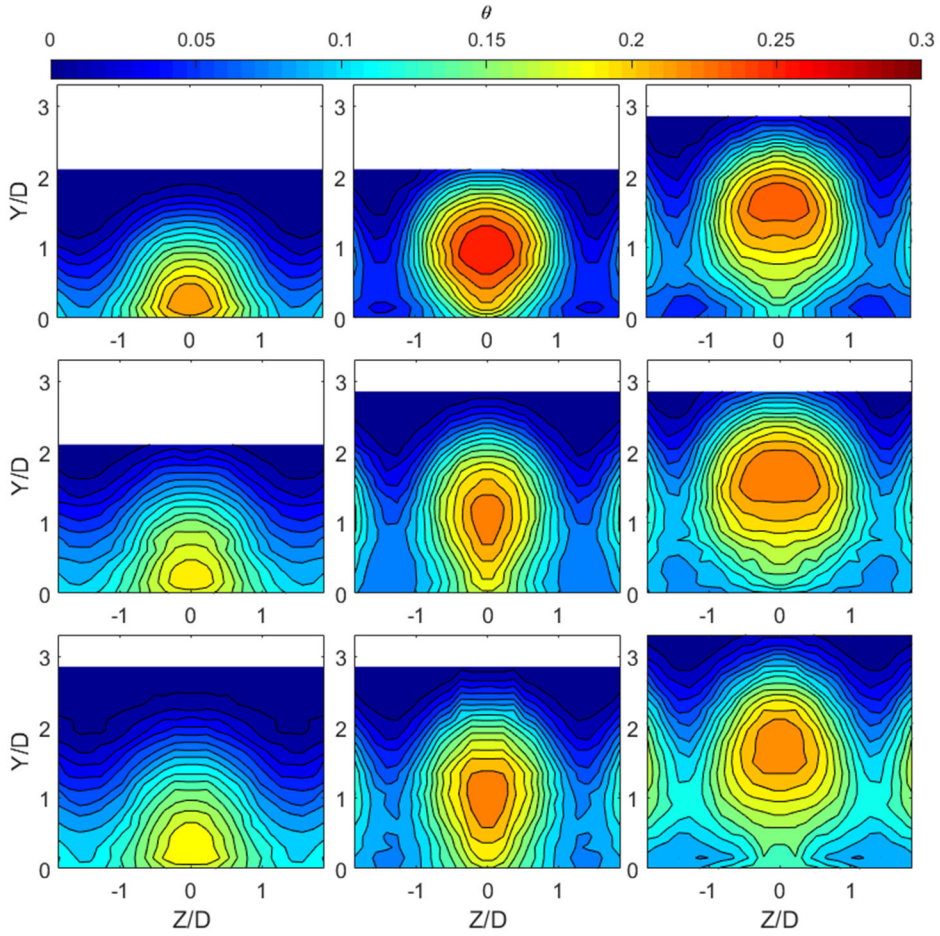

Figure 28: Coolant jet temperature cross sections at x = 18D, in θ temperature units, under the following conditions: from left to right M = 0.5, 1.0, and 1.5, and from top to bottom K = 0, -0.5×10^{-6}, -0.68×10^{-6}.

Particle Image Velocimetry (PIV) was used to collect velocity fields of the jet cross sections at x = 10D. From these fields turbulence and swirl could also be extracted. Figure 29 displays the velocity vector field overlaid onto a contour plot of the turbulence intensity. Turbulence intensity is the ratio of the root mean square of the velocity fluctuations over the mean velocity for that time, as described previously. In these plots the spanwise component of the turbulence is displayed. The biggest influencer on the turbulence and velocity behavior is the changing blowing ratio. In all the cases there are two, counter rotating vortices in each coolant jet, as described previously. As blowing ratio increases the strength of these vortices increases. Turbulence increases significantly when the blowing ratio increases to M = 1.5. The coolant jets pull away from the wall with increased blowing ratio, as is also seen in Figures 25, 26, and 27. As the magnitude of deceleration increases there is little change in the behavior of the coolant jets. They appear to pull away from the wall slightly with increased deceleration, but the effect is small.

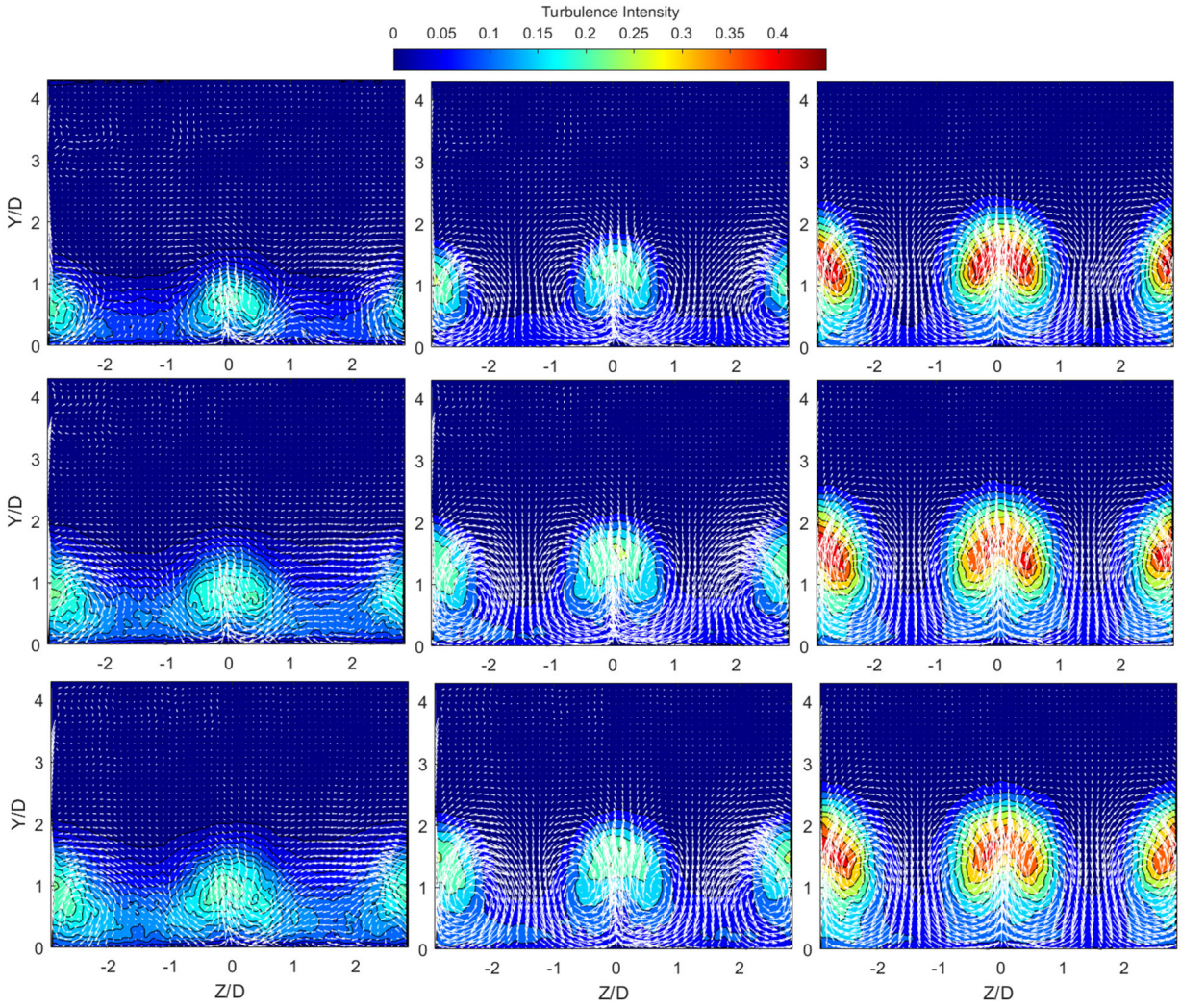

Figure 29: Coolant jet cross section velocity field overlaid on to the turbulence intensity contour plot at x = 10D, under the following conditions: from left to right M = 0.5, 1.0, and 1.5, and from top to bottom K = 0, -0.5×10^{-6}, -0.68×10^{-6}.

Figure 30 shows the same velocity fields as Figure 29, however, they are overlaid onto contour plots of the swirl. This is a measure of the vorticity of the coolant jet cross section. Positive swirl corresponds to rotation in the clockwise direction and negative swirl to rotation in the counter clockwise direction. The counter rotating vortices are evident in the swirl plot with the red and blue portions that fall on either side of the center of the coolant jets. In the $M = 0.5$ case the vortices are weak and barely visible. Increasing blowing ratio to $M = 1.0$ causes the vortices to increase in

strength significantly, with a further increase in strength occurring at M = 1.5. There is no discernable change of the vortices between deceleration magnitudes.

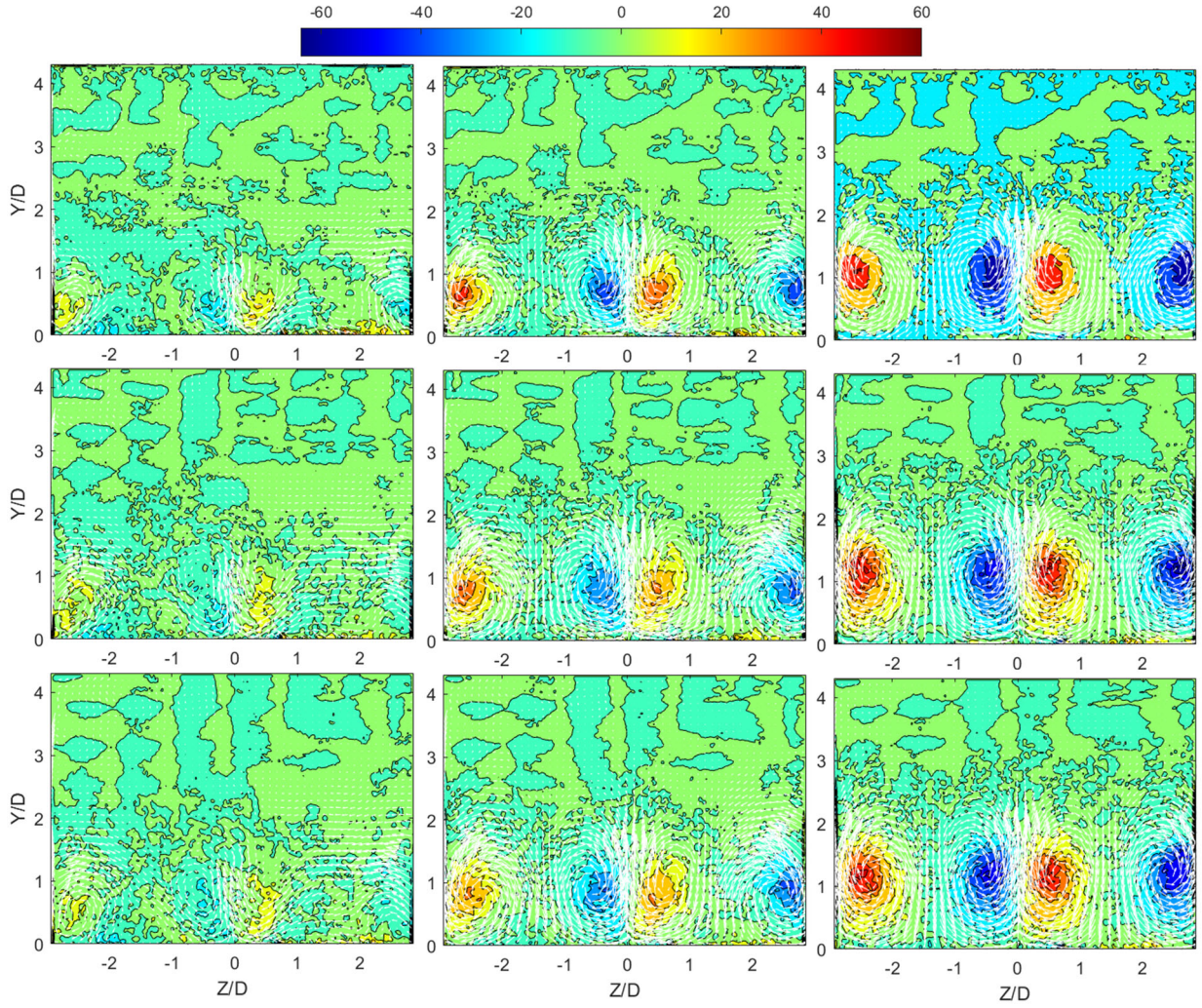

Figure 30: Coolant jet cross section velocity field overlaid on to the swirl contour plot at x = 10D, under the following conditions: from left to right M = 0.5, 1.0, and 1.5, and from top to bottom K = 0, -0.5×10^{-6}, -0.68×10^{-6}.

Velocity, turbulence, and temperature profiles were collected upstream and downstream of the coolant holes at all three acceleration parameters without the coolant jets. All of the profiles shown below were taken at the spanwise centerline of the test wall (z = 0). Figure 31 displays the velocity profiles both upstream and downstream of the coolant holes. The upstream profiles show that the

boundary layer is thicker for the two decelerated cases. There is a noticeable difference between the $K = 0$ profile and the decelerated profiles, however, the profiles at $K = -0.5\times10^{-6}$ and $K = -0.68\times10^{-6}$ are very similar. The general trend is the same for the downstream profiles, but the differences in the profiles for each acceleration parameter are more noticeable.

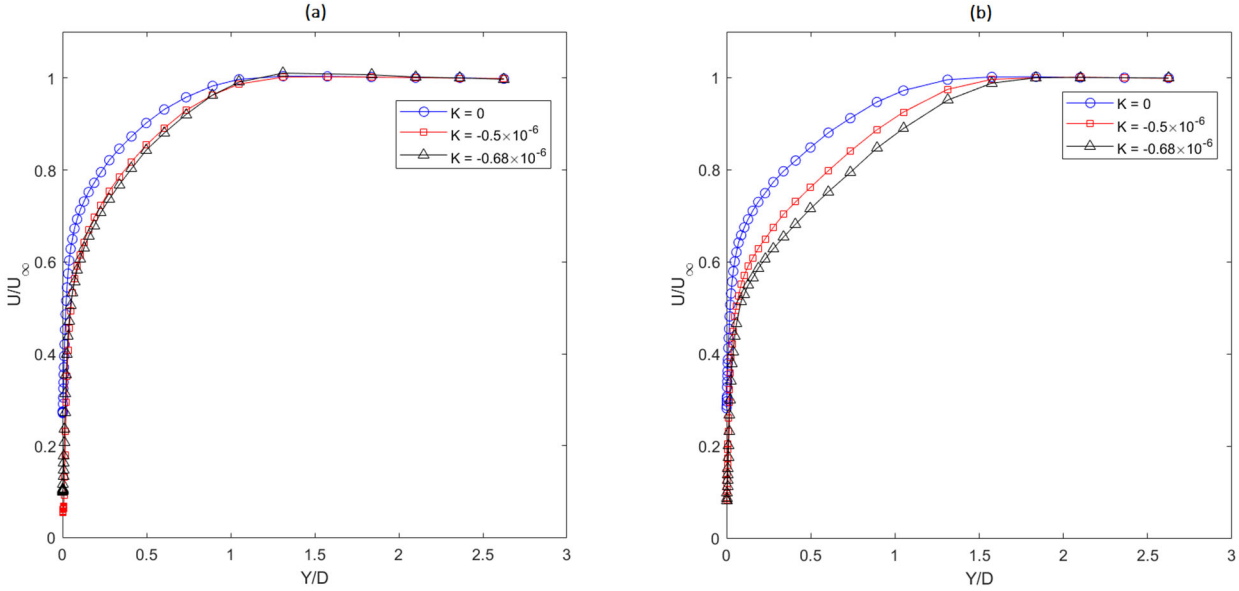

Figure 31: Velocity profiles (a) upstream at x = -3.22D and (b) downstream at x = 12D with no jets.

As mentioned previously, the Law of the Wall was used to pull some quantitative data from the profile shape. Table 4 displays these results. As the magnitude of deceleration is increased the boundary layer thickness, momentum thickness, and momentum thickness Reynolds number increases, and the skin friction coefficient decreases.

Figure 32 displays the turbulence profiles taken upstream and downstream of the coolant holes. This turbulence intensity is the streamwise component of turbulence. Upstream of the holes the turbulence intensities peak at 11.9%, 13.0%, and 11.6% for acceleration parameter values of $K = 0$, -0.5×10^{-6}, and -0.68×10^{-6}, respectively. Downstream of the holes the turbulence intensities

peak at 11.5%, 12.4%, and 10.9%, respectively. At both distances the decelerated cases take longer to fall to the freestream turbulence level. These differences are most apparent in the downstream profile. This is expected because the boundary layer becomes thicker as the air is decelerated, resulting in higher turbulence intensities farther out from the wall.

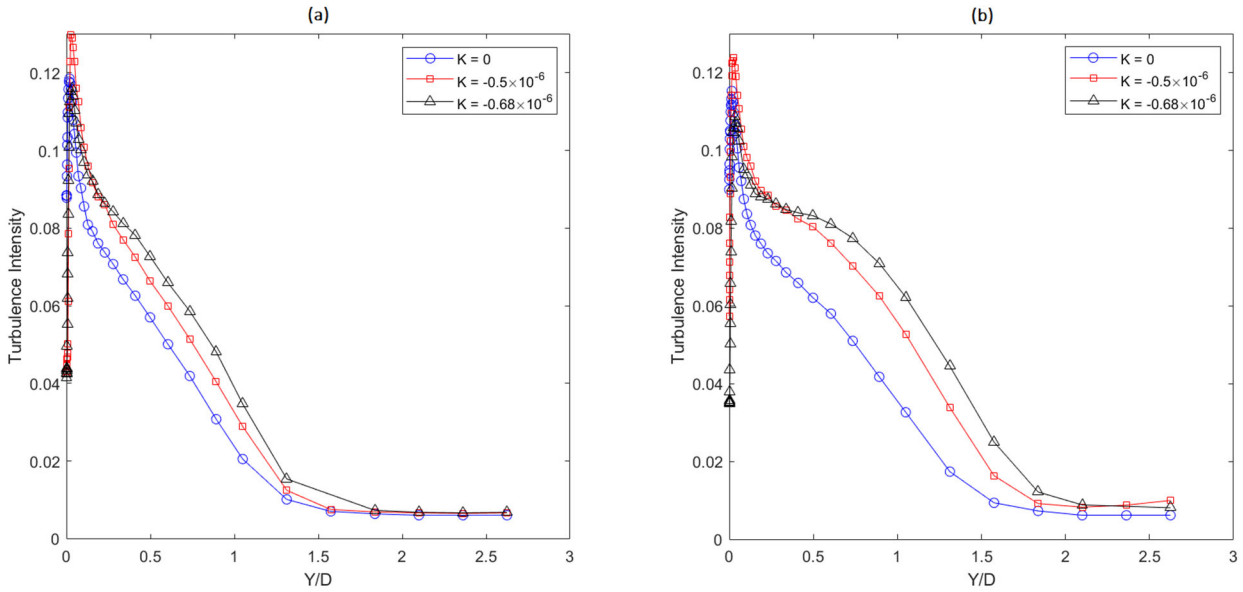

Figure 32: Turbulence profiles (a) upstream at x = -3.22D and (b) downstream at x = 12D with no jets.

Figure 33 displays temperature profiles taken upstream and downstream of the coolant holes without jets. The walls were heated during these temperature measurements. Because there were no jets blowing during these temperature profiles, θ is not useful for representing non-dimensional temperature. Instead, β is used for these temperature profiles.

$$\beta = \frac{T_w - T}{T_w - T_\infty} \tag{13}$$

Equation 13 defines β, where T_w is the wall temperature, T is the temperature at a point, and T_∞ is the freestream temperature. The upstream temperature profiles have little difference between the three acceleration parameters. The downstream profiles show that the two decelerated cases have produce a thicker thermal boundary layer than the $K = 0$ case.

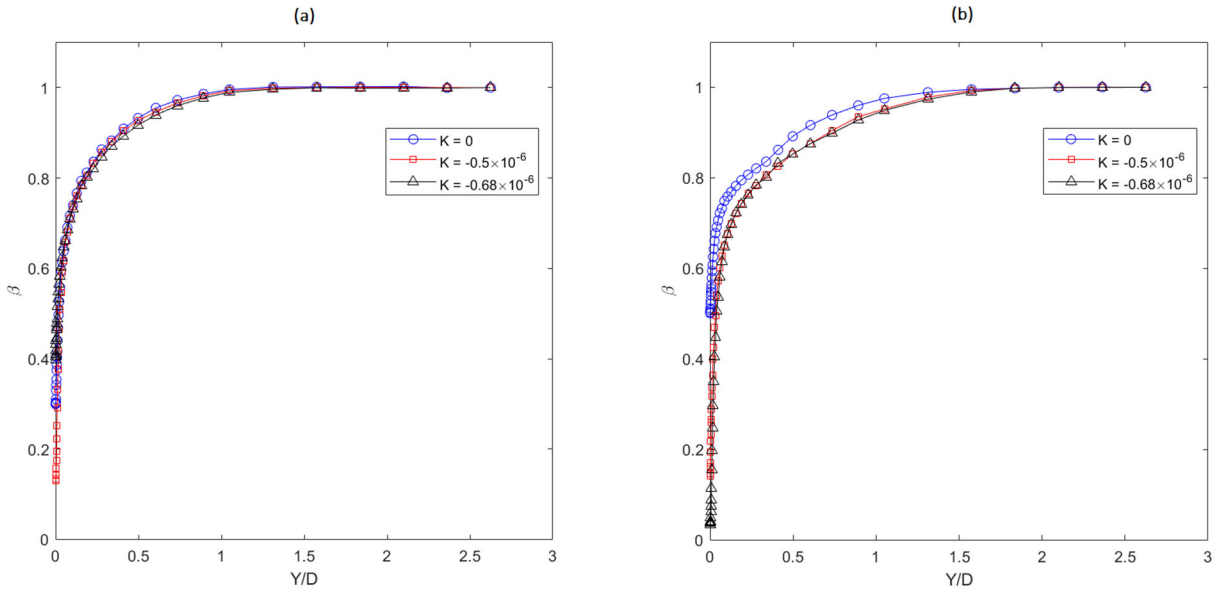

Figure 33: Temperature profiles (a) upstream at x = -3.22D and (b) downstream at x = 12D with no jets and wall heaters on.

Table 5 displays quantitative results calculated from the temperature profiles using the thermal law of the wall. Wall temperature, thermal boundary layer thickness, and enthalpy thickness tend to increase, while Stanton number tends to decrease, as the magnitude of deceleration is increased, but the effect is small. The Stanton number at the downstream location remains the same throughout the three acceleration parameters. The enthalpy thickness Reynolds number shows no trend when comparing different acceleration parameters. The thermal boundary layer thickness, wall temperature, and Stanton number remain similar throughout the changing acceleration parameter. The fact that the Stanton numbers at the different acceleration parameters converge to the same value as they move downstream is consistent with the Stanton number ratio plots in Figure 24. These Stanton numbers were compared to the values obtained from the IR camera data over the same condition to ensure that they were similar. Table 6 contains these comparisons.

Table 6: Wall temperature and Stanton number comparison across collection methods.

Acceleration Parameter	Blowing Ratio	Downstream Coordinate	Stanton Number	
			From Profile	From IR Data
0	0	12D	2.3×10^{-3}	2.3×10^{-3}
-0.50×10^{-6}	0	12D	2.3×10^{-3}	2.3×10^{-3}
-0.68×10^{-6}	0	12D	2.3×10^{-3}	2.8×10^{-3}

Velocity and turbulence profiles were also collected at the downstream coordinate x = 12D while the coolant jets were running at blowing ratios of M = 0.5, 1.0, and 1.5. Figure 34 shows the velocity profiles taken. These profiles appear to have two individual profiles in each plot. There is an increase in velocity from the wall to the jet, and then another increase from the jet to the freestream. As blowing ratio increases the first level off occurs at a greater velocity, and the profile stays level for a greater distance. The thicker boundary layer created by the deceleration of the air can be seen most notably in the M = 0.5 and 1.0 profiles. In the M = 1.5 profiles the different acceleration parameters have little effect on profile shape.

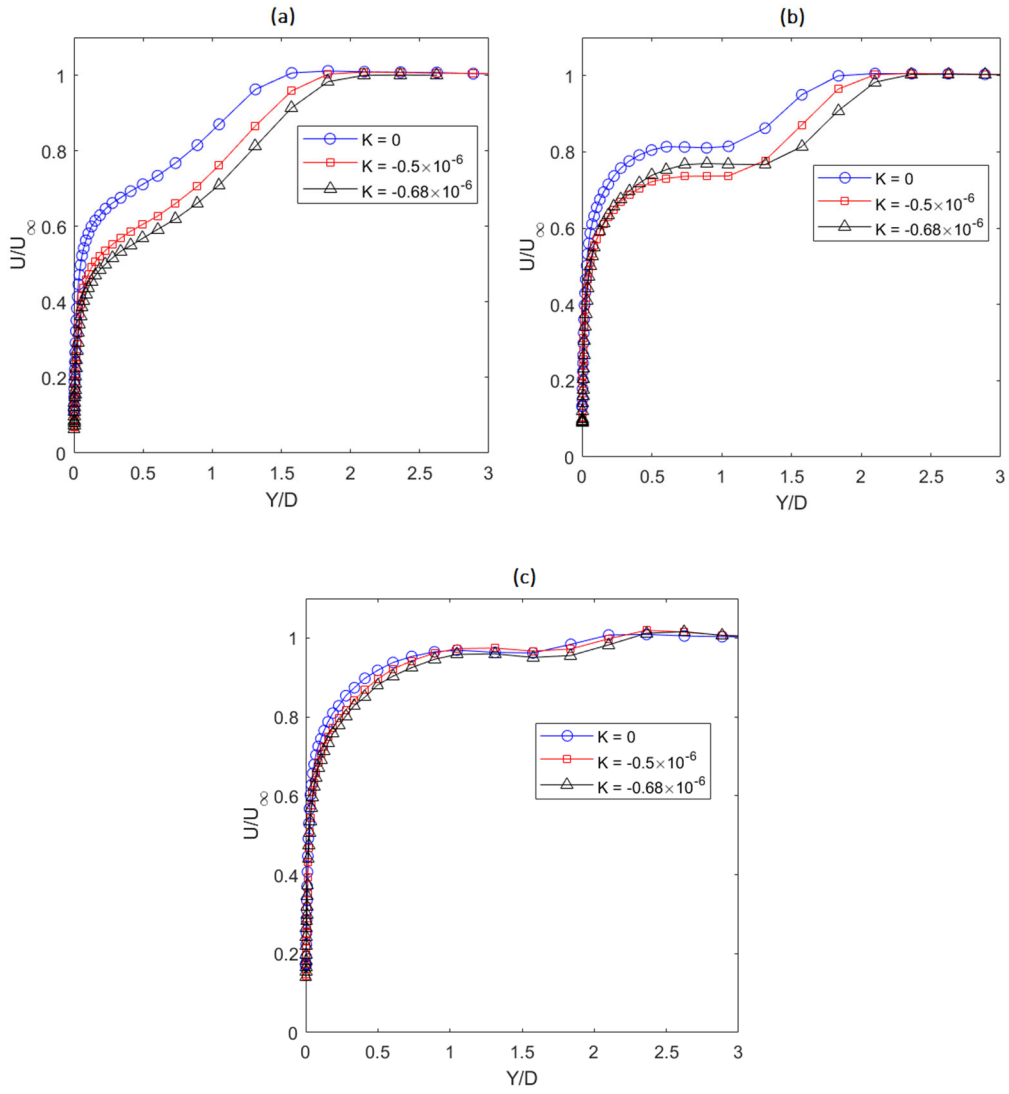

Figure 34: Velocity profiles downstream x = 12D with jets at (a) M = 0.5, (b) M = 1.0, and (c) M = 1.5.

The turbulence intensity profiles with coolant jets are shown in Figure 35. These show the streamwise component of turbulence. The turbulence intensity comes to a maximum close to the wall, similar to Figure 32, and then decreases until it enters the coolant jets, where the turbulence rises. The turbulence intensity within the coolant jets decreases with respect to the maximum turbulence intensity as blowing ratio increases. There are noticeable humps in the profiles at M = 0.5 and 1.0, but no hump at M = 1.5. Instead the turbulence levels off temporarily. As the magnitude of deceleration increases, turbulence intensity increases at all blowing ratios. At all

blowing ratios, an increase in the magnitude of deceleration causes the secondary turbulence intensity peak to occur farther away from the wall and at a greater magnitude. This is consistent with previous results because the deceleration pulls the jets away from the wall, and induces greater turbulence within the freestream and coolant jet flows.

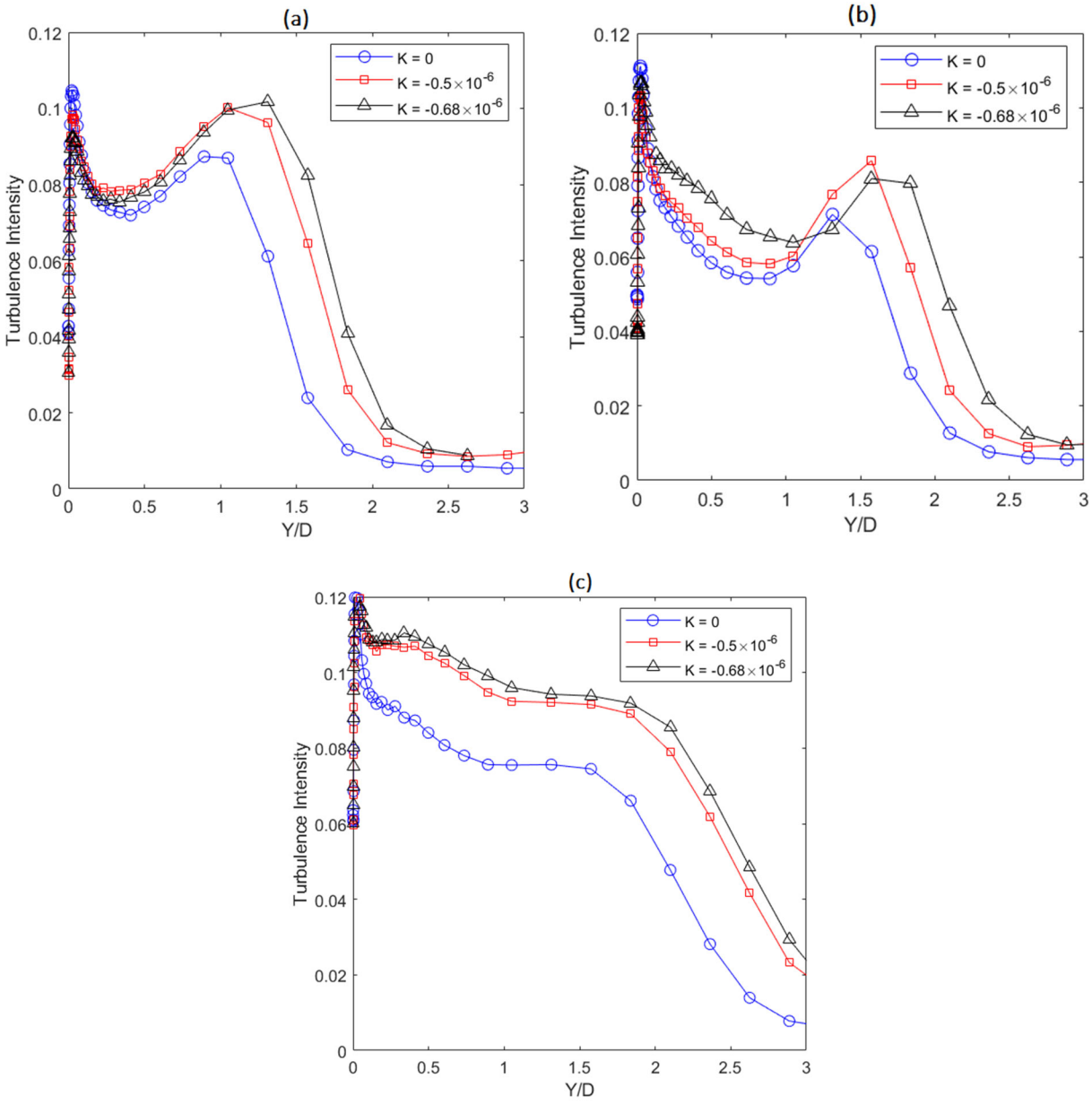

Figure 35: Turbulence profiles downstream at x = 12D with jets at (a) M = 0.5, (b) M = 1.0, and (c) M = 1.5.

Figure 36 displays temperature profiles measured at the downstream coordinate of x = 10D with the coolant jets running. These profiles are extracted out of the cross-section temperature surveys

shown in Figure 27. These plots increase in temperature initially as Y/D increases because the coolant jets are higher temperature than the freestream flow. They reach a maximum and begin to decrease in temperature as the probe moves out of the coolant jet and into the freestream flow. The decelerated cases have a lower maximum temperature, and their maximum temperature occurs further away from the wall than the $K = 0$ cases. This is expected because the deceleration disperses the coolant jets, lowering their temperature. At $M = 1.5$ the difference between the different acceleration parameters is the smallest.

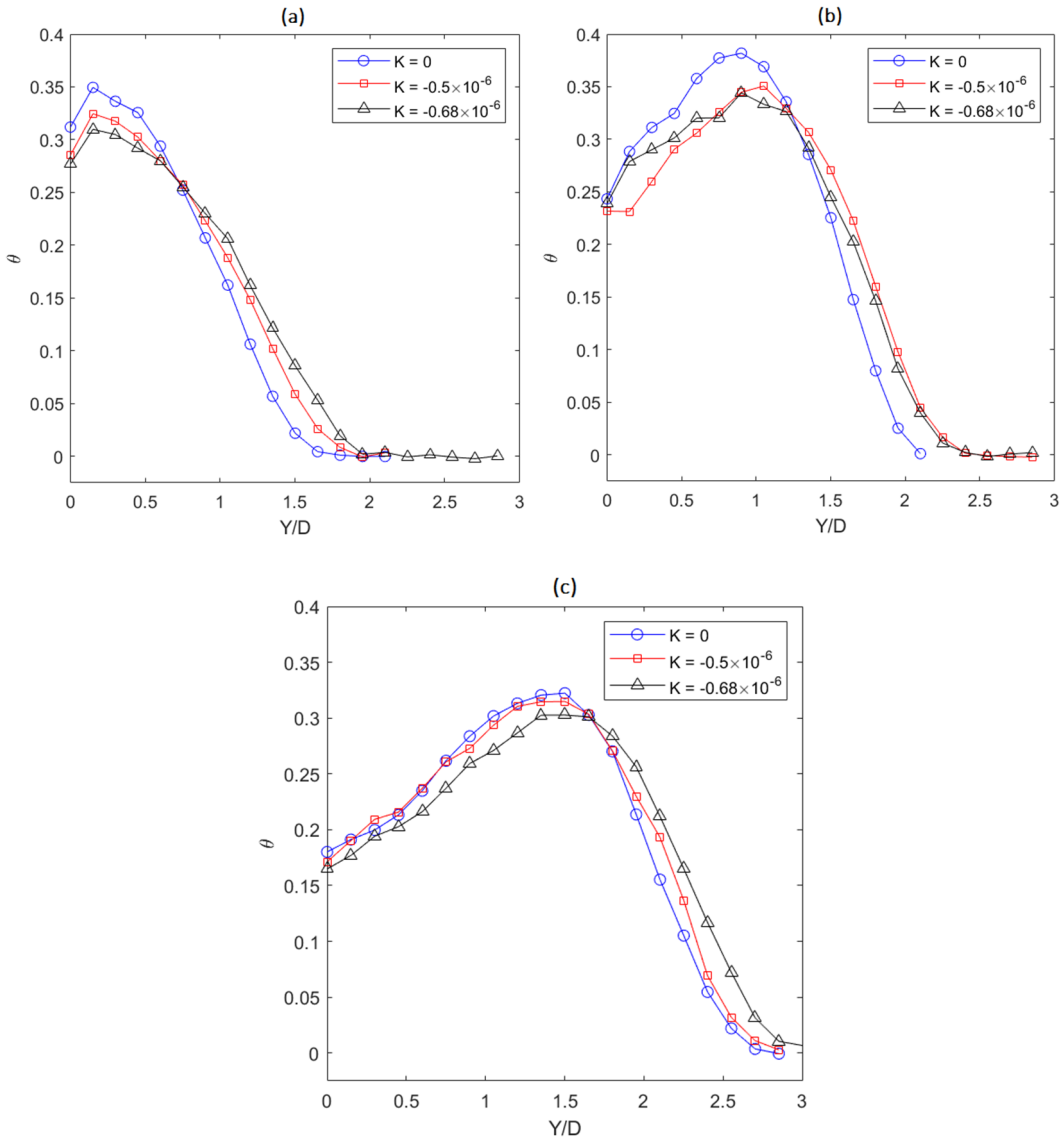

Figure 36: Temperature profiles downstream at x = 10D with jets at (a) M = 0.5, (b) M = 1.0, and (c) M = 1.5.

Table 6 displays a comparison of the Stanton numbers extracted from the temperature profiles to those calculated from the IR camera data. Under the same conditions the Stanton numbers are consistent in all cases except for the $K = -0.68\times10^{-6}$ case. In this case there is a 20% difference in the Stanton number values. This could be due to the noise seen in the Stanton number data from the IR camera. As is shown in Figures 23 and 24, the $K = -0.68\times10^{-6}$ data is not as clean as the $K = 0$ and -0.50×10^{-6} case.

Table 7 displays comparisons between film effectiveness measured with the IR camera, and the non-dimensional temperature θ taken near the wall using thermocouples. The average percent difference across all the cases and locations is 21.47%. This is a large difference, however, the non-dimensional temperature θ and film cooling effectiveness of the wall are not being measured in the same place. The IR data provide the temperature of the wall, while the thermocouples measure the temperature of the flow close to the wall. This comparison is most useful for ensuring that the two data points are following the same trends throughout the cases, which they do. Tables 6 and 7 provide additional confidence that the data were collected and analyzed in a consistent fashion across collection methods.

Table 7: Film effectiveness comparison across collection methods.

Acceleration Parameter	Blowing Ratio	Downstream Coordinate	Non-Dimensional Temperature	Centerline Film Effectiveness	Percent Difference
0	0.5	2D	0.698	0.723	3.56
		10D	0.312	0.403	25.5
		18D	0.208	0.275	27.7
	1	2D	0.378	0.374	0.903
		10D	0.244	0.282	14.7
		18D	0.161	0.198	20.6
	1.5	2D	0.165	0.195	16.6
		10D	0.180	0.244	30.1
		18D	0.126	0.198	44.3
-0.50×10^{-6}	0.5	2D	0.627	0.687	9.19
		10D	0.285	0.353	21.1
		18D	0.183	0.230	22.9
	1	2D	0.334	0.341	2.17
		10D	0.232	0.258	10.6
		18D	0.175	0.188	7.46
	1.5	2D	0.204	0.147	32.7
		10D	0.171	0.205	18.1
		18D	0.103	0.166	46.9
-0.68×10^{-6}	0.5	2D	0.528	0.660	22.2
		10D	0.277	0.386	33.0
		18D	0.177	0.270	41.7
	1	2D	0.368	0.248	39.0
		10D	0.239	0.269	11.9
		18D	0.174	0.205	16.0
	1.5	2D	0.160	0.092	53.4
		10D	0.165	0.176	6.55
		18D	0.131	0.132	0.753

Conclusion

The purpose of this study is to isolate the effects of freestream deceleration on gas turbine film cooling to gain a better understanding of this phenomenon. This knowledge will increase understanding of film cooling flows and contribute to the creation of more accurate models of gas turbine flow. More accurate models will allow film cooling to be optimized, further increasing gas turbine efficiency and power output. Results show that freestream deceleration at K values of -0.50×10^{-6} and -0.68×10^{-6} decreases centerline film effectiveness by 3% and 11%, respectively, at their peaks, at a blowing ratio of 1.5. These peaks occur at low downstream distances. The $M = 1.5$ case is the only case where freestream deceleration effects were outside the measurement

uncertainty range. All other cases showed no significant effect of freestream deceleration on film cooling effectiveness. There were no significant effects of freestream deceleration on Stanton number ratio. In conclusions, this study shows that freestream deceleration has little to no effect on film cooling effectiveness and Stanton number ratio. Analyzing the flow characteristics with temperature, velocity, and turbulence profiles, as well as temperature surveys, velocity fields, swirl contour plots, and turbulence contour plots shows small changes in the flow with deceleration. The most noticeable effect is the thicker boundary layers caused by deceleration, but coolant jet behavior changes little between deceleration magnitudes. Recording the changes in the flow and establishing how they relate to film effectiveness and Stanton number allow more accurate models to be produced. The lack of an effect allows models to be simplified because cases of freestream deceleration can be approximated as zero acceleration cases. This is another step closer to a fuller understanding of film cooling and how it is influenced under various conditions.

References

[1] "Open Cycle Gas Turbines." IPIECA, February 1, 2019. http://www.ipieca.org/resources/energy-efficiency-solutions/power-and-heat-generation/open-cycle-gas-turbines/.

[2] Moody, M. "Jet Engine HP Turbine Blade." Pinterest. Accessed November 3, 2019. https://www.pinterest.com/pin/566679565582855743/?lp=true.

[3] Bogard, D. G., and Thole, K. A., "Gas Turbine Film Cooling." *Journal of Propulsion and Power* 22, Vol. 2, 2006, pp. 249–270.

[4] Teekaram, A., Forth, C., and Jones, R., "Film Cooling in the Presence of Mainstream Pressure Gradients," *Journal of Turbomachinery*, Vol. 113, 1991, pp. 484–492.

[5] Brown, A., and Saluja, C. L., "Film Cooling from a Single Hole and a Row of Holes of Variable Pitch to Diameter Ratio," *International Journal of Heat and Mass Transfer*, Vol. 22, 1979, pp. 525–533.

[6] Lutum, E., Von Wolfersdorf, J., Semmler, K., Dittmar, J., and Weigand, B. "An Experimental Investigation of Film Cooling on a Convex Surface Subjected to Favourable Pressure Gradient Flow." *International Journal of Heat and Mass Transfer*, Vol. 44, 2001, pp. 939–951.

[7] Lutum E, Von Wolfersdorf, J., Semmler, K., Naik, S., and Weigand, B. “Film cooling on a concave surface: influence of external pressure gradient on film cooling performance.” NATO/AGARD symposium on advanced flow management, Norway, 2001.

[8] Ryan, K. J., Coletti, F., Elkins, C. J., and Eaton, J. K. “Building Block Experiments in Discrete Hole Film Cooling.” *ASME Paper GT2015–43731,* 2015.

[9] Maiteh, B. Y., and Jubran B. A. “Effects of Pressure Gradient on Film Cooling Effectiveness from Two Rows of Simple and Compound Angle Holes in Combination.” *Energy Conversion and Management* Vol. 9-10, 2004, pp. 1457–1469.

[10] Schmidt, D. L., and Bogard, D. G. “Pressure Gradient Effects on Film Cooling.” *ASME Paper 95-GT-018,* 1995.

[11] Jessen, Wilhelm, Konopka, M., and Schroeder, W. “Particle-Image Velocimetry Measurements of Film Cooling in an Adverse Pressure Gradient Flow.” *Journal of Turbomachinery*, Vol. 134, 2011, paper 021025.

[12] Womack, K. M., Volino, R. J., and Schultz, M. P. Combined Effects of Wakes and Jet Pulsing on Film Cooling. *Journal of Turbomachinery,* Vol. 130, 2008, paper 041010.

[13]Pelzer, C. S., and Volino, R. J. The Effects of Acceleration on Film Cooling in Gas Turbine Engines. *Trident Scholar Committee*, Report No. 499, 2020.

[14] Kays, W. M., and Crawford, M. E. *Convective Heat and Mass Transfer* (3rd ed.) New York City, NY: McGraw-Hill, 1980.

[15] Coulthard S. M., Volino, R. J., and Flack, K. A. Effect of Jet Pulsing on Film Cooling: Part 1— Effectiveness and Flowfield Temperature Results. *Journal of Turbomachinery*, Vol. 129, 2007, pp. 232-246.

[16] Coulthard S. M., Volino, R. J., and Flack, K. A. Effect of Jet Pulsing on Film Cooling—Part II: Heat Transfer Results. *Journal of Turbomachinery*, Vol. 129, 2007, pp.247-257.